ELECTRICAL RESISTIVITY OF HOT-PRESSED COMPACTS

by

THIAGARAJAN RAMANAN
B.Sc. (Physics), University of Madras, India, 1965.
B.E. (Metallurgy), I.I.Sc., Bangalore, India, 1968.

A THESIS SUBMITTED IN PARTIAL FULFILMENT
OF THE REQUIREMENTS FOR THE DEGREE OF
MASTER OF APPLIED SCIENCE

in the Department

of

METALLURGY

We accept this thesis as conforming to the
standard required from candidates for
the degree of Master of Applied Science

Members of the Department
of Metallurgy

THE UNIVERSITY OF BRITISH COLUMBIA

May, 1970

In presenting this thesis in partial fulfilment of the requirements for

an advanced degree at the University of British Columbia, I agree that

the Library shall make it freely available for reference and study.

I further agree tha permission for extensive copying of this thesis

for scholarly purposes may be granted by the Head of my Department or

by his representatives. It is understood that copying or publication

of this thesis for financial gain shall not be allowed without my

written permission.

Department of _____ Metallurgy _____

The University of British Columbia
Vancouver 8, Canada

Date June 9, 1970 _____

ABSTRACT

An attempt has been made to study the change in the electrical resistivity of a powder compact during the initial stages of hot-pressing. Theoretical models have been formulated on the basis of plastic deformation of spheres in a compact. The resistivity change during densification has been derived for various packing arrangements. For small deformation of spheres, the final equation is

$$\frac{\sigma_m}{\sigma_c} = \alpha \left[\left(\frac{D}{D_o} \right)^{2/3} - 1 \right]$$

and the more generalized equation for larger deformation is

$$\frac{\sigma_m}{\sigma_c} = \alpha \left(D^{2/3} \beta^{2/3} R^2 - 1 \right)$$

where σ_m and σ_c are the conductivities of a compact of spheres having a relative density D, and at the theoretical density ($D = 1$), respectively. D_o is the initial relative density of the compact before deformation. α is a constant depending on geometry and R is the radius of spheres at any stage of deformation in arbitrary units. The derived relationship was tested by: (a) measuring the electrical resistivity as a function of density during hot-pressing of compacts of glass spheres, (b) measuring the electrical resistivity of different compacts of nickel spheres at room temperature, and (c) comparing previous resistivity data with the theoretical equation.

ACKNOWLEDGEMENTS

TABLE OF CONTENTS

TABLE OF CONTENTS (continued)

LIST OF FIGURES

LIST OF FIGURES (continued).

LIST OF FIGURES (continued)

LIST OF TABLES

I. INTRODUCTION

Sintering[1] is a complex process by which densification of a powder compact takes place at a temperature below the melting point of the (bulk of the) material. Hot-pressing[2] is a sintering process, in the presence of an applied pressure. Hot-pressing methods promise products of greater density at much lower temperatures and for shorter times than conventional sintering processes.

The degree of densification during and after sintering or hot-pressing can be determined in several ways, some of which are listed below:

1) measurement of density changes,

2) measurement of strength,

3) microscopic examination,

4) electrical measurement,

5) thermal conductivity determination,

6) sound velocity determination,

7) X-ray diffraction analysis, etc.

Density determination is the most widely used technique. For small objects, this does not pose any problem, but for large pieces such as those fabricated by hot-or cold-rolling, hot-or cold-extrusions, density measurement is not easy and frequently involves destruction of the objects. Measurements of strength and thermal characteristics are difficult and are of low precision,when porous bodies of very low strength are to be measured. Microscopic observations show very little change during early stages of sintering. Measurement of sound velocity is

fairly complicated as are X-ray diffraction measurements.

Compared with all these methods, measurements of electrical properties, such as electrical resistivity and temperature coefficient of resistance, have many advantages. They can be made with fairly simple equipment. Because of the much greater change in resistivity than in density, they are excellent indicators in early stages of sintering when other methods can be applied only with a low degree of precision or with great difficulty.

I.1. PREVIOUS ELECTRICAL RESISTIVITY MEASUREMENTS

The earliest work in this field was that of Trzebiatowski[3], who reported a rapid decrease in electrical resistivity of sintered copper and gold compacts with increase in temperature and density. This work was followed by that of Iwase and Ogawa[4], Myers[5], Huttig[6], Adlassnig and Foglar[7] etc.. Hausner[8] studied the behaviour of copper and nickel powders, hot-pressed in hydrogen at 5 to 80 t.s.i. in the temperature range 600°C to 1000°C. He plotted the electrical resistivity as a function of density and compacting pressure at various temperatures. (Figures 1 and 2). He noted a difference in the electrical resistivity at a given density for powders of different sizes, both in the as-compacted stage and hot-pressed condition. The electrical resistivity of the green compact was found to be a function of the particle size.

Kimura and Hisamatsu[9] carried out sintering studies on copper and nickel powders in hydrogen, argon and vacuum. They plotted the electrical resistivity as a function of temperature in different atmospheres, (Figure 3), and noted different steps in the resistivity
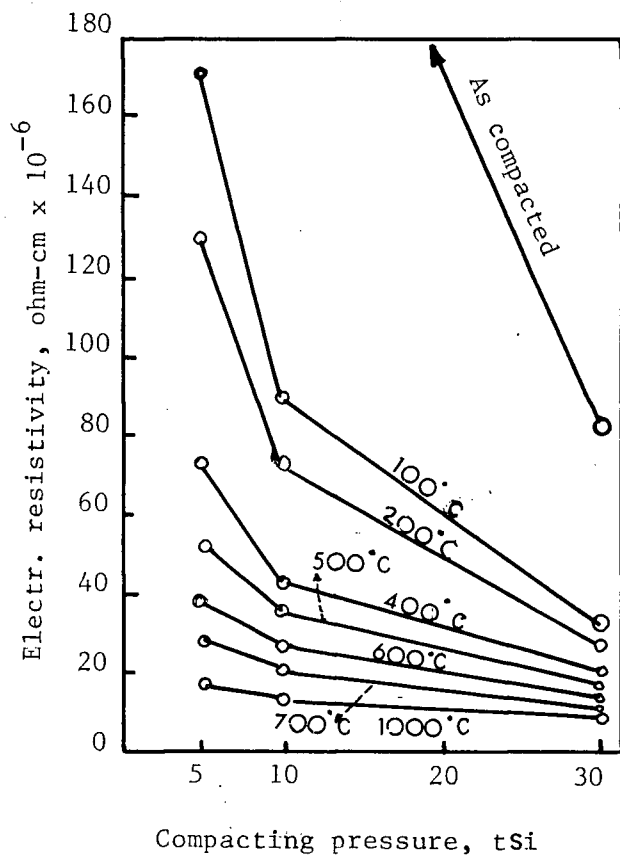
Figure 1.

Effect of compacting
pressure on the
electrical resistivity
of coarse (75 -100μ)
carbonyl nickel powder
compacts during
sintering (After Hausner[8]).

Figure 2.

Electrical resistivity
vs. density of coarse
and fine (<44μ)
carbonyl nickel powder
compacts heated in
hydrogen from 600° to
1100°C (After Hausner[8]).
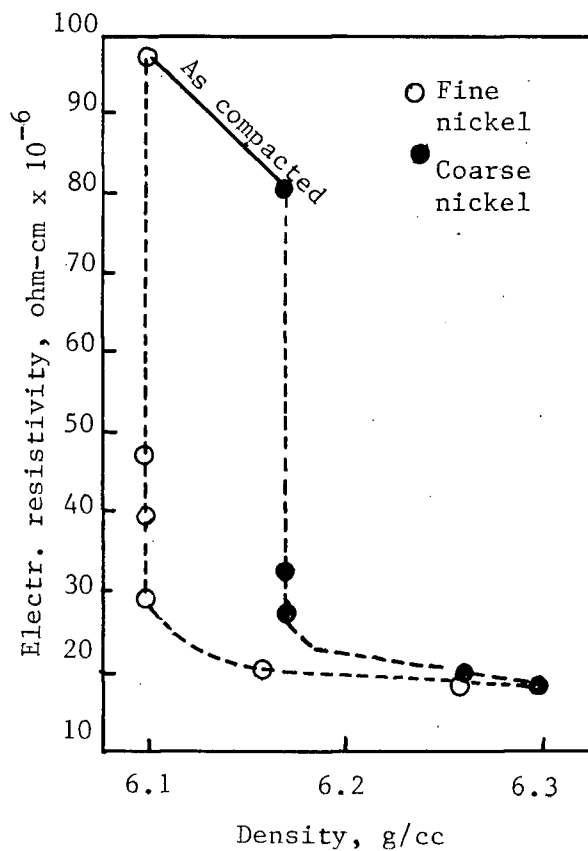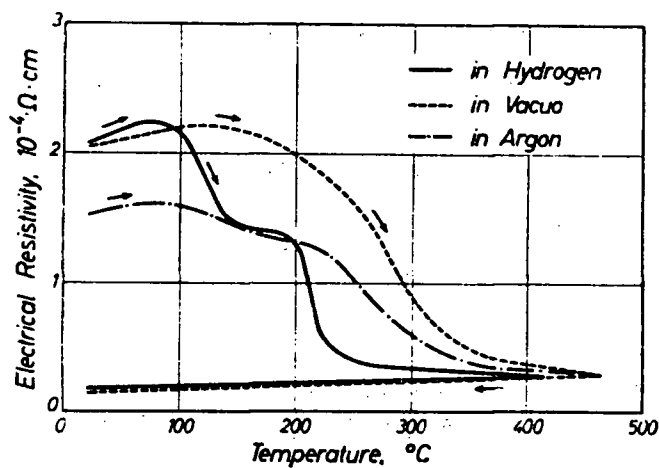
Figure 3. Effect of atmosphere on change of
electrical resistivity in raising
temperature of copper compacts.
(After Kimura[9]).
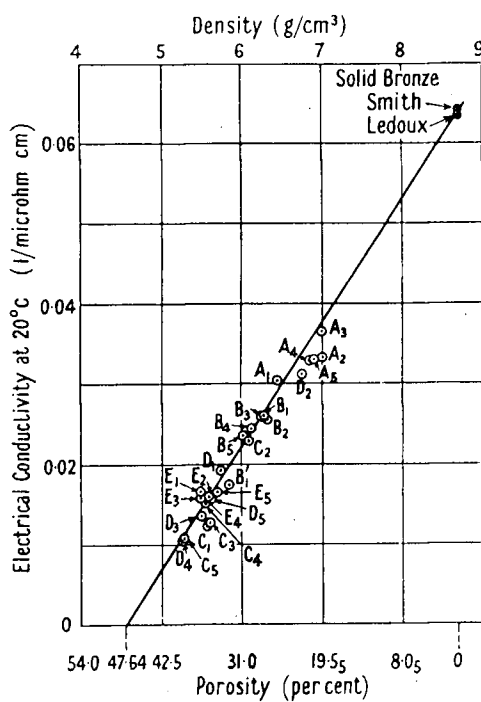
Figure 4. Porous bronze : variation of
electrical conductivity (20°C) with
density. A_1, A_2 etc refer to porous
bronze specimens. (After Grootenhuis[10]).

curves, in agreement with Myers' work[5]. In hydrogen, two steps of
rapid decrease were observed. In argon and vacuum, only one step
was observed. The first step in hydrogen at low temperature could be
due to the reduction of the surface oxide layer or removal of adsorbed
gases. The subsequent step at higher temperature (in all atmospheres)
is due to sintering and bonding of metal powders.

Grootenhuis et al[10] studied the electrical resistivity
of sintered bronze (Figure 4). They replotted the works of others[3, 7,
8,11 to 15] on copper and nickel powders (Figures 5 & 6), and claimed
that in all cases the experimental data conformed to the straight line,
drawn from the point for solid metal to cut the x-axis at a porosity
of 47.6%. This porosity corresponds to the maximum porosity, which can
be attained on packing equal sized spheres in simple cubic array.
Consequently, zero conductivity was assumed for a simple cubic packing
of spheres, and the increase in conductivity with density was attributed
to increase in contact area between particles, and increasing interparticle
bonding. The rather large scatter in the result was caused by
difficulties in obtaining the data from various figures in the publications,
and the difference in quality of the specimens used by the investigators.

I.2. QUANTITATIVE APPROACH

All these studies (so far listed) have been qualitative
in nature. A rigorous mathematical approach to predict accurately
the conductivity of porous compacts from the known conductivity values
of the solid materials was not available. This is primarily due to the
fact that the packing geometry of the random shaped powders is very
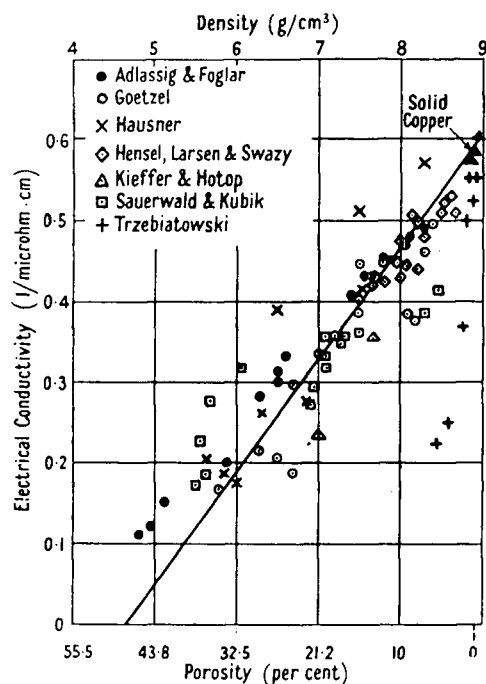
Figure 5. Porous copper: electrical
conductivity at $20^{\circ}C$
(After Grootenhuis[10]).
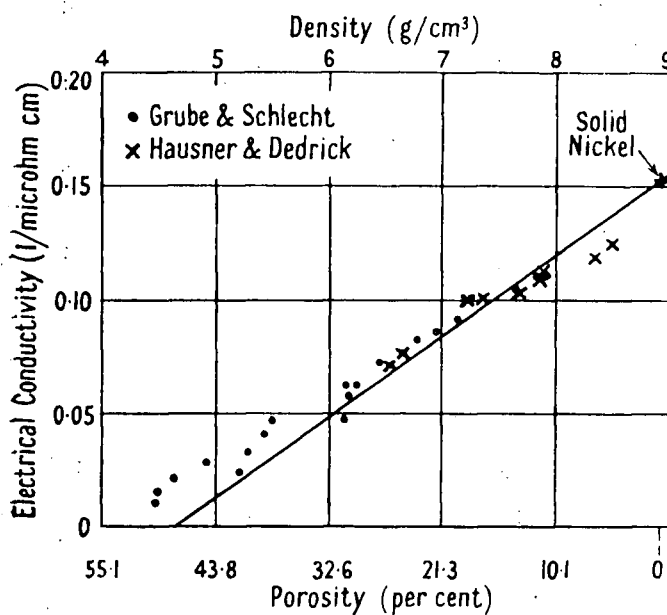
Figure 6. Porous nickel: electrical conductivity
at $20^{\circ}C$ (After Grootenhuis[10]).

complicated and it is very difficult to predict the resistivity of such a network. However, the studies carried out on the thermal and electrical conductivities of two phase systems, in terms of the volume fractions of the two phases, have thrown much light in this field. The equations derived for two phase systems, in many cases, allow one to closely estimate the electrical conductivity of porous sintered materials, by assuming one of the phases to be the pore phase.

A simplified approach is to consider the material as having a regular orientation and a structure, such as the parallel slabs, shown in Figure 7. If the current flow is parallel to the plane of the slabs, they are equivalent to a parallel electrical circuit. The total conductivity of the material σ_m is given by

$$\sigma_m = V_1 \sigma_1 + V_2 \sigma_2 \qquad - - - - - - - - (1)$$

where V_1 and V_2 are the volume fractions (equal to cross-sectional area) and σ_1 and σ_2 are the conductivities of each component.

i.e. $\dfrac{\sigma_m}{\sigma_2} = (1 - V_2) \dfrac{\sigma_1}{\sigma_2} + V_2$

If $\sigma_2 >> \sigma_1$, for example, component 1 being air,

$$\frac{\sigma_m}{\sigma_2} = V_2 \qquad - - - - - - - - (2)$$

If the slabs are arranged normal to current flow, they are equivalent to a series electrical network and

$$\frac{1}{\sigma_m} = \frac{V_1}{\sigma_1} + \frac{V_2}{\sigma_2}$$
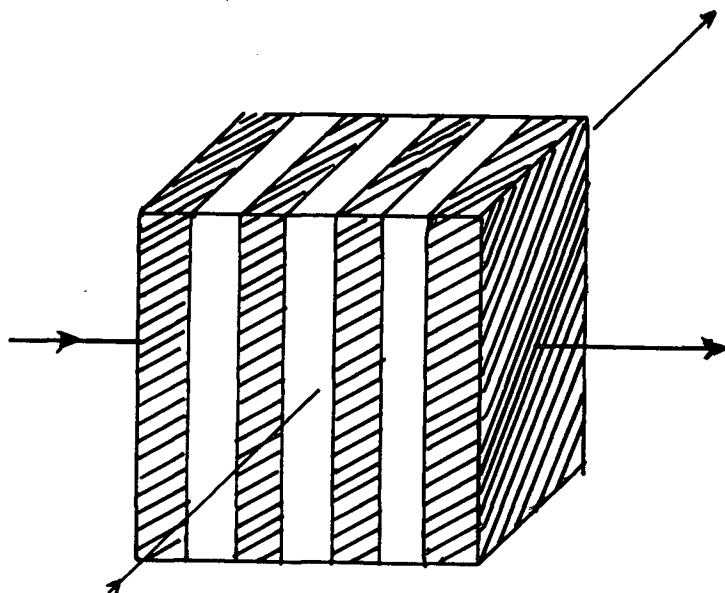
Figure 7.

Geometric distribution of phases (parallel slabs) and directions of current-flow.

Figure 8.

Conductivity curves for parallel and series circuits of a two-phase system. Maxwell's equation for spherical inclusion is also included. ($\sigma_2 = 10\sigma_1$ assumed).
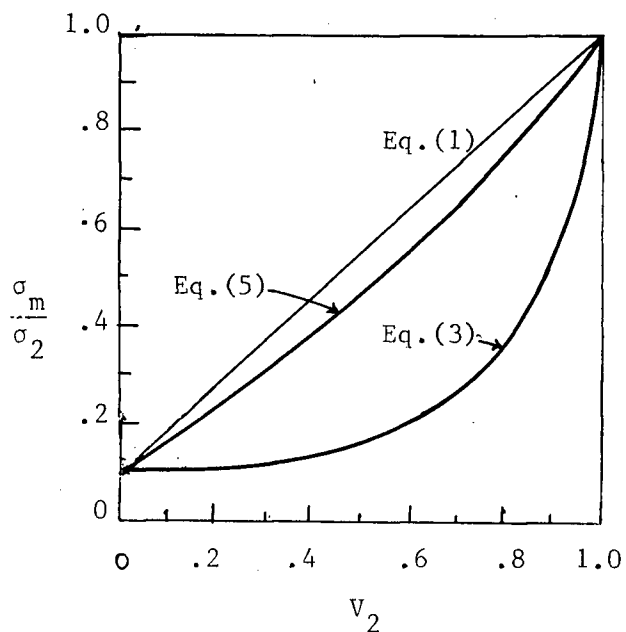
or $\quad \sigma_m = \dfrac{\sigma_1 \sigma_2}{V_1 \sigma_2 + V_2 \sigma_1}$ $\quad - - - - - - - - - - -$ (3)

and $\quad \dfrac{\sigma_m}{\sigma_2} = \dfrac{1}{V_2 + (1-V_2)\dfrac{\sigma_2}{\sigma_1}}$

If $\sigma_2 \gg \sigma_1$,

$$\frac{\sigma_m}{\sigma_2} = \frac{\sigma_1/\sigma_2}{(1-V_2)} \qquad - - - - - - - - - - - \text{(4)}$$

In Figure 8 , equations (1) and (3) are plotted for $\sigma_2 = 10\sigma_1$.

Huttig[22] has shown that all conductivity data on sintered porous materials should fall within the region bounded by the two curves, given by equations (2) and (4). These two equations define the upper and the lower bounds for conductivity data (Figure 9).

The above equations are idealised. In practice, it is essential to use equations derived for random spherical inclusions in a continuous matrix phase, or spherical particles in a continuous minor phase. Relationships applicable to random mixtures have been derived by various authors from Maxwell's equation[16] for a continuous matrix phase σ_2, with spherical dispersed phase σ_1. The conductivity of the mixture σ_m is given by[16]

$$\frac{\sigma_m - \sigma_2}{\sigma_m + 2\sigma_2} = \frac{V_1(\sigma_1 - \sigma_2)}{\sigma_1 + 2\sigma_2} \qquad - - - - - - - - - \text{(5)}$$
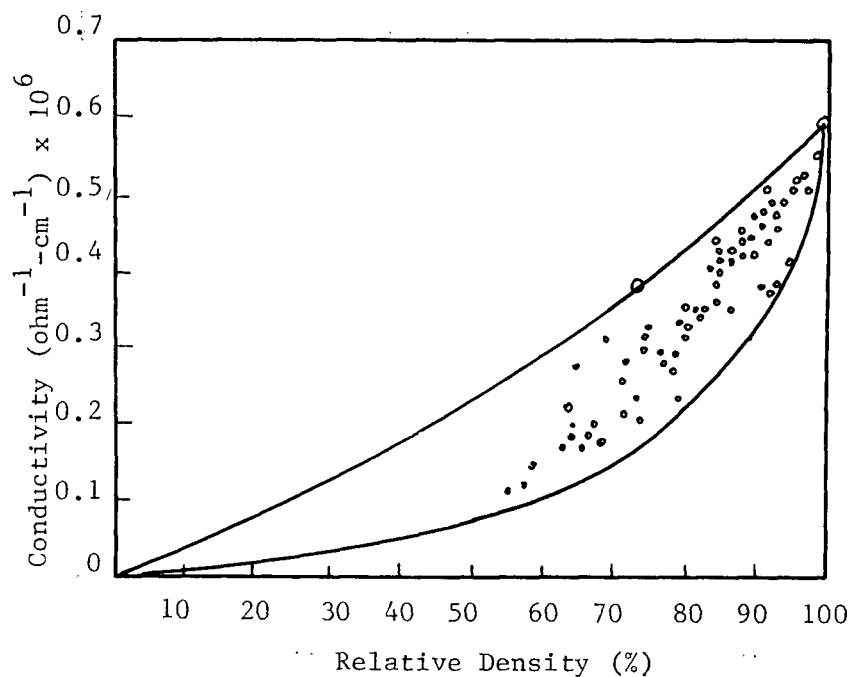
Figure. 9. Change in conductivity with relative density for pressed copper powder (After Huttig[22]).
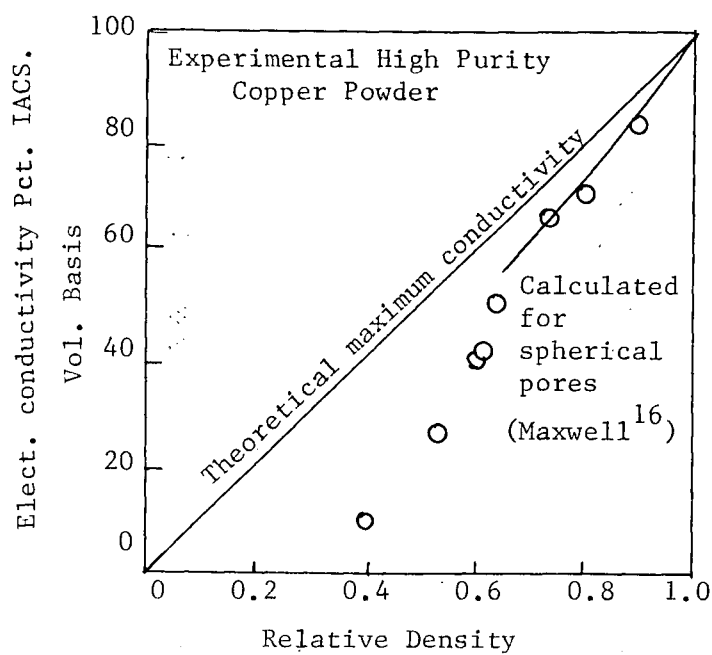
Figure 10. Measured and calculated electrical conductivities of high-purity sintered copper specimens (After Klar[21]).

V_1 and V_2 are the volume fractions of the dispersed and matrix phases. When $\sigma_2 \gg \sigma_1$, for example, phase 1 being spherical pores,

$$\sigma_m = \sigma_2 \ \frac{1 - V_1}{1 + V_1/2}$$

$$= \sigma_2 \ \frac{2(1 - V_1)}{2 + V_1} \quad - - - - - - - - - - - - \ (6)$$

Equation (5) is included in Figure 8 and is found to satisfy some of the experimental results. Similar equations derived by Juretschke et al[17], Doebke[18], Torkar[19], and Grekila and Tien[20], all starting from Maxwell's relation[16], are shown in Table I. These equations are converted for applying to porous compacts and are also included in the table. All these equations are found to hold good only for certain sets of data, and for the final stages of sintering and hot-pressing. For instance, Klar and Michael[21] tested the equations on sintered copper powder and found good agreement with Maxwell's equation (equation (6)), but only at higher densities (> 80% bulk density), as shown in Figure 10.

Mal'ko et al[23] and Litvinenko et al[24] have considered another set of equations for the electrical conductivity of porous metal compacts, which are listed below:

$$\sigma_m = \sigma_2 \ \frac{(2 - 3V_1)}{2} \quad \text{------------ (a)}$$

$$\sigma_m = \sigma_2 \ \frac{1 - V_1}{1 + V_2} \quad \text{------------ (b)}$$

$$\sigma_m = \frac{3}{2} V_2 \sigma_1 \frac{0.9 - V_1}{2.1 + V_1{}^2} \quad\text{————————— (c)}$$

They were developed using Odelevskii's[22] formulae for statistical mixtures and matrix systems. These equations are similar to those listed in Table I. Equation (a) was found to fit their experimental results satisfactorily at higher densities.

I.3. OBJECTIVES OF THE PRESENT WORK

A literature survey reveals that there is no satisfactory equation to predict the electrical conductivity of a powder compact during the initial stages of sintering or hot-pressing. Investigations carried out so far during the early stages of densification merely point out, that the experimental data scatter around a linear rate of increase of electrical conductivity with increasing density of hot-pressed compacts. Towards the end of hot-pressing, however, Maxwell's and other similar equations have successfully predicted the variation of the relative electrical conductivity $\frac{\sigma_m}{\sigma_2}$ with the relative density (or volume fraction V_2; density of phase 1 – air – can be considered to be negligible).

The purpose of this investigation is:

a) to derive an equation to predict the conductivity of a porous compact as a function of its relative density in the range 0.6 to 0.75. Compacts of relative density 0.6 to 0.75 constitute the early stages of densification during sintering and hot-pressing, and

b) to test the derived equation with experimental data for validity.

TABLE I

ELECTRICAL CONDUCTIVITY EQUATIONS FOR TWO-PHASE COMPOSITES

	Equation for Two-phase System	Equation for Porous Body	Comments	Reference
A.	$\dfrac{\sigma_m - \sigma_2}{\sigma_m + 2\sigma_2} = \dfrac{V_1(\sigma_1 - \sigma_2)}{\sigma_1 + 2\sigma_2}$	$\sigma_m = \dfrac{2\sigma_2(1 - V_1)}{2 + V_1}$	Spherical Inclusions	Maxwell[16]
B.	$\dfrac{\sigma_m - \sigma_2}{\sigma_m + \sigma_2} = \dfrac{V_1(\sigma_1 - \sigma_2)}{\sigma_1 + \sigma_2}$	$\sigma_m = \dfrac{\sigma_2(1 - V_1)}{2 + V_1}$	Cylindrical Inclusions	Juretschke[17]
C.	$\dfrac{\sigma_m - \sigma_1}{\sigma_m + K\sigma_2} = \dfrac{V_2(\sigma_2 - \sigma_1)}{\sigma_2(1 + K)}$	$\sigma_m = \dfrac{K\sigma_2(1 - V_1)}{K + V_1}$	K is a Function of σ_2/σ_1	Doebke[18]
D.	$\dfrac{\sigma_m - \sigma_2}{\sigma_m + K(\sigma_1^2 + \sigma_2^2)^{1/2}}$ $= \dfrac{V_2(\sigma_2 - \sigma_2)}{\sigma_1 + K(\sigma_1^2 + \sigma_2^2)^{1/2}}$	$\sigma_m = \dfrac{K\sigma_2(1 - V_1)}{K + V_1}$	Inter-Penetrating Phases	Torkar[19]
E1.	$\sigma_m = \dfrac{\sigma_2(AV_2 - B)}{(C - V_2)}$ for $V_2 > 0.25$	Same as two-phase system	Tetrakaideca-hedron Model	
E2.	$\sigma_m = \sigma_1 \dfrac{1}{(1 - V_2)}$ for $V_2 < 0.25$	Same as Two-phase system	Tetrakaideca-hedron Model	Grekila and Tien[20]

A, B and C = constants.

σ_m = electrical conductivity of the compact,

σ_1 and σ_2 = electrical conductivity of the pore and matrix phases,

V_1 and V_2 = Volume fraction of the pore and matrix phases.

II. THEORETICAL DEVELOPMENTS.

II.1. GEOMETRIC RELATION AND CURRENT NETWORK

In the development of the theory, it is assumed that the particles in a compact are monosized spheres (because a sphere is the simplest and most symmetric shape) and that they are arranged in a regular three-dimensional array. During hot-pressing, they deform plastically at the points of contact and form flat faces. The compact density change as a result of this deformation, with respect to contact radius, has been derived by Kakar[26] and is given by

$$D = \frac{1}{\beta (R^2 - a^2)^{3/2}} \quad ---------- \quad (7)$$

where D is the bulk-density of the compact at contact radius 'a'. R is the instantaneous radius of the particle at neck radius 'a' and β is a geometric constant which depends on the packing configuration.

First, consider the geometry of deformation of two spheres in contact (Figure 11). Let the two spheres constitute an electrical path. The equivalent resistances are shown. In the initial period of deformation, the neck region will have a much higher resistance, r_2, (neglecting contact resistance) as compared to the resistance r_1 of the spheres. Hence, the conductivity of the circuit will depend upon the neck area πa^2 and the thickness of the neck G (boundary width). The total current path is (G + 4y'). The boundary width G can be assumed to remain constant during neck growth and as G << 4y', the total path length 4y' ≃ 4y.
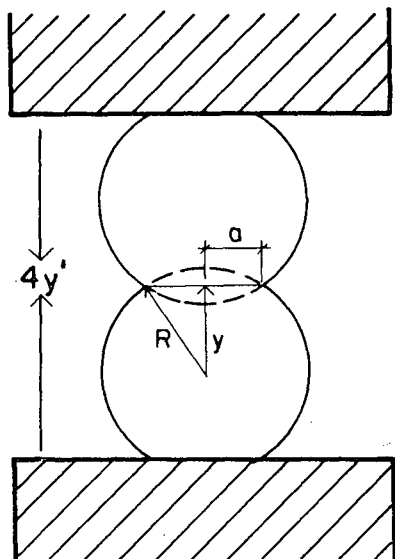
DEFORMATION OF
TWO SPHERES
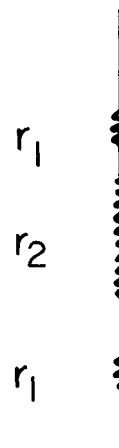
EQUIVALENT ELECTRICAL
NETWORK

Figure 11. Geometry of deformation of two spheres in contact and
equivalent electrical network.
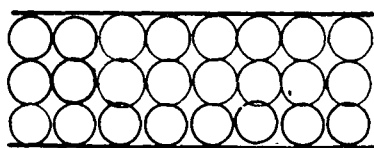
TWO DIMENSIONAL (CUBIC)
ARRAY OF SPHERES
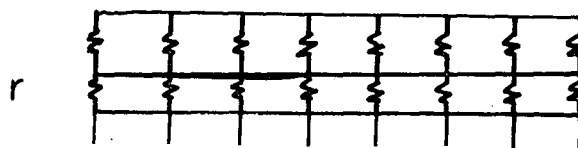
EQUIVALENT ELECTRICAL
NETWORK

Figure 12.. Spheres in two-dimensional cubic array and equivalent
electrical network.

The spheres can be arranged in a two dimensional cubic network, as shown in Figure 12 . The corresponding resistance circuit is also shown. If r is the resistance of each neck region, a vertical column of spheres in Figure 12 will have a resistance of 2r (neglecting resistance of the sphere). If there are n spheres in a horizontal row, they constitute n parallel paths. As there is no flow of current along a horizontal direction, the resistance of the network becomes $\frac{2r}{n}$. If there are N stacking of spheres, each column will have a resistance of $(N - 1)r \simeq Nr$ (since $N \gg 1$, $N - 1 \simeq N$). The circuit resistance becomes $\frac{N}{n} r$. The principle can be extended to spheres arranged in a three-dimensional array. Each sphere can now be contained in a unit cell. The specific resistance of this unit cell is the same as for the spheres packed in three dimensions.

II.2. THEORETICAL MODELS

The basic systems of packing which give rise to space-filling unit cells can be summarised as follows:[29] (1) simple cubic (Z = 6), (2) orthorhombic (Z = 8), (3) body-centered cubic (Z = 8), and (4) rhombohedral (Z = 12), where Z is the coordination number. Of these the b.c.c. packing is an unstable arrangement in a unidirectional field of force (i.e. gravitational force). However, the b.c.c. packing gives rise to a tetrakaidecahedron unit cell which has been extensively used in the theoretical models for sintering[1], grain growth etc.. For theoretical purposes, it is assumed that each type of packing is stable and maintains its symmetry on application of pressure, and that the material at the points of contact spreads symmetrically during deformation to maintain the sphericity of the particle. The different modes of packing are shown in the Appendix.

II.3. GEOMETRIC RELATIONSHIPS

a) Simple Cubic Packing

Consider a cubic array of spheres, deformed under uniform hydrostatic pressure along the three mutually perpendicular directions. Each sphere will have six flat faces formed as shown in Figure 13. The unit cell in this case is a cube of side 2y, where $y = (R^2 - a^2)^{1/2}$.

The number of current-paths through the unit cell = 1.

The area of current-flow = πa^2 and

The path-length = $2y = 2(R^2 - a^2)^{1/2}$.

The conductivity of the unit cell, $1/R_m$ (where R_m = resistivity) is given by

$$\frac{1}{R_m} = \frac{1}{R_c} + \frac{1}{R_i} \quad - - - - - - - - - - - - - \quad (8)$$

where $\dfrac{1}{R_c}$ = conductivity of the solid, viz. sphere,

and $\dfrac{1}{R_i}$ = conductivity of the insulating phase filling the

rest of the unit cell, which is air in the case

of porous compacts.

Now,

$$\frac{1}{R_m} = \frac{A_c}{L_c}\,\sigma_c + \frac{A_i}{L_i}\,\sigma_i \quad - - - - - - - - - \quad (9)$$

where A_c and A_i are the areas of current-flow, L_c and L_i are the path-lengths, and σ_c and σ_i are the specific conductivities. Subscripts c and i stand for conducting and insulating phases, respectively.

As $\sigma_i \to o$ (for air), equation (9) reduces to

$$\frac{1}{R_m} = \frac{A_c}{L_c}\,\sigma_c \quad - - - - - - - - - - - - \quad (10)$$
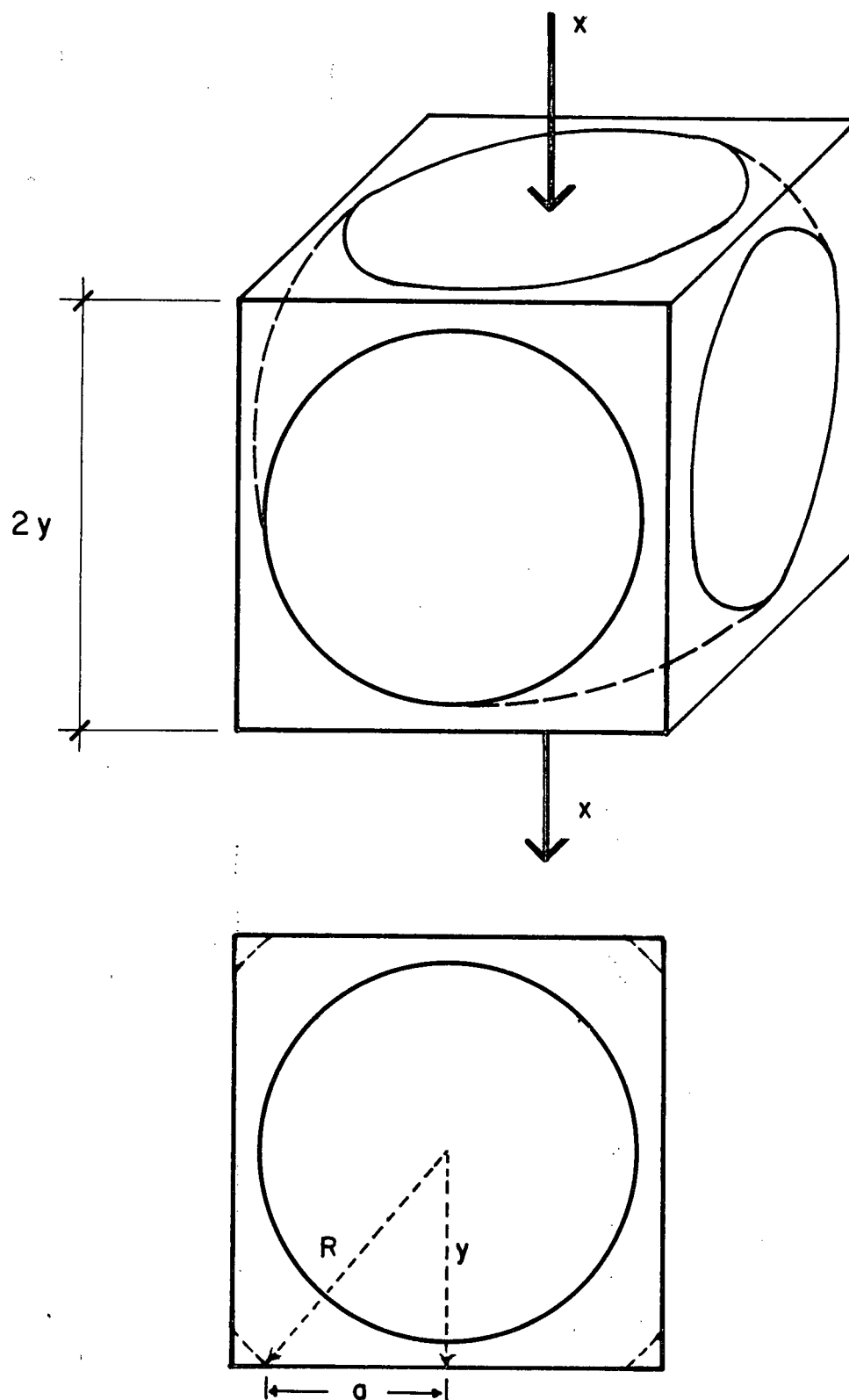
Figure 13. Geometric relationship of simple cubic model and current-path (x - x).

For the cubic cell,

$$\frac{1}{R_m} = \frac{\pi a^2}{2y} \sigma_c \quad .$$

The specific conductivity of the unit cell σ_m is

$$\sigma_m = \frac{L_s}{A_s} \times \frac{1}{R_m} \qquad - - - - - - - - - - -(11)$$

where L_s is the length of the unit cell,

and A_s is the area of the unit cell normal to current-flow.

Substituting for $\frac{1}{R_m}$ in equation (11) from equation (10), we get

$$\sigma_m = \frac{L_s}{A_s} \cdot \frac{A_c}{L_c} \cdot \sigma_c$$

i.e.

$$\frac{\sigma_m}{\sigma_c} = \frac{L_s}{L_c} \cdot \frac{A_c}{A_s} \qquad - - - - - - - - - - - - (12)$$

For the cubic cell, $L_s = 2y$ and $A_s = 4y^2$.

Hence the relative conductivity is

$$\frac{\sigma_m}{\sigma_c} = \frac{2y}{2y} \cdot \frac{\pi a^2}{4y^2}$$

$$\frac{\sigma_m}{\sigma_c} = \frac{\pi}{4} \quad \frac{a^2}{R^2 - a^2} \qquad - - - - - - - - - - - - - (13)$$

b) Orthorhombic Packing

Each sphere after deformation will have eight faces. The deformed sphere for this model and its unit cell are shown in Figure 14.
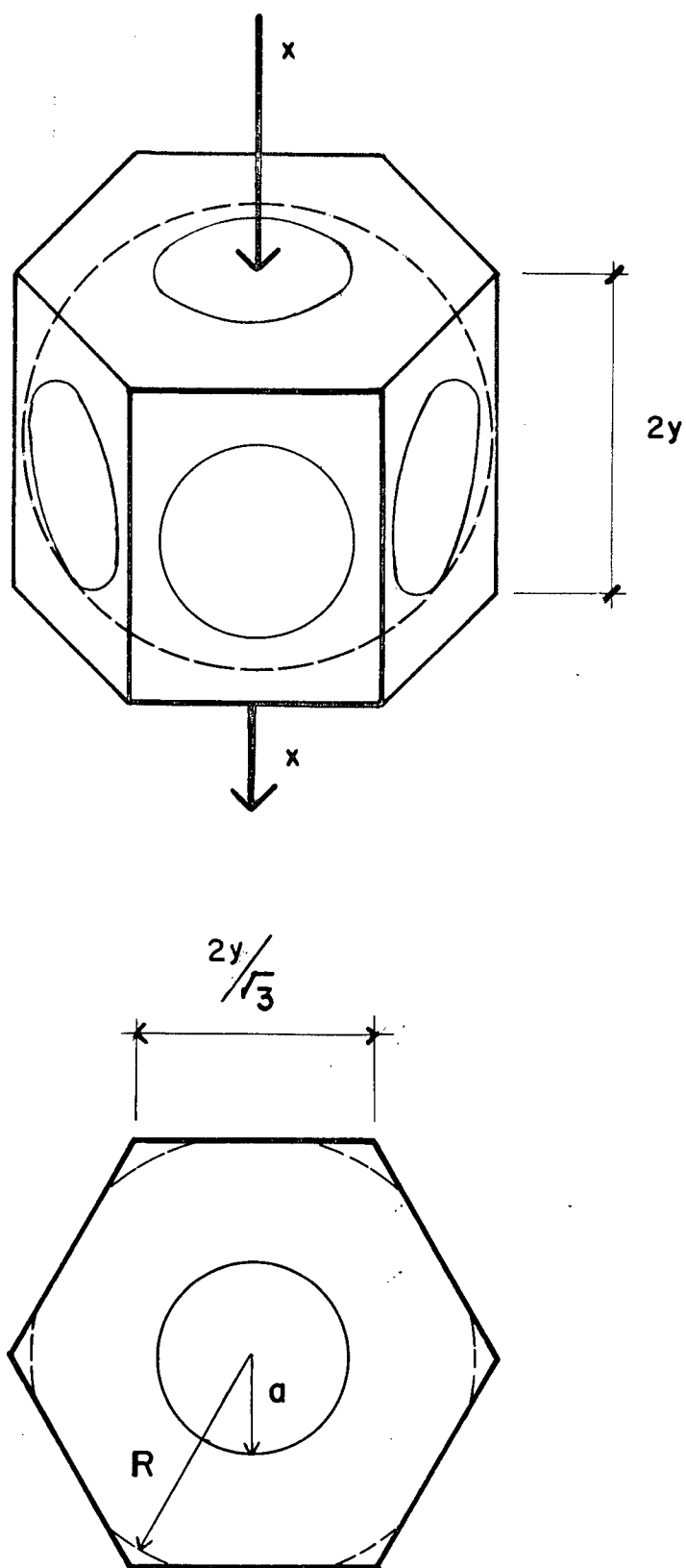
Figure 14. Geometric relationship of orthorhombic model and current-path (x – x).

In this case,

the number of current-paths = 1,

the area of current-flow = $\pi a^2 = A_c$,

and path-length = $2y = L_c$.

For the unit cell, $L_s = 2y$

$$A_s = 2\sqrt{3}y^2.$$

Hence,

$$\frac{\sigma_m}{\sigma_c} = \frac{L_s}{L_c} \cdot \frac{A_c}{A_s} \qquad \text{(equation 12)}$$

$$= \frac{2y}{2y} \cdot \frac{\pi a^2}{2\sqrt{3}y^2}$$

$$\frac{\sigma_m}{\sigma_c} = \frac{\pi}{2\sqrt{3}} \frac{a^2}{(R^2 - a^2)} \quad -------(14)$$

c) **Rhombohedral Packing***

(F.C.C. and H.C.P Packing)

Each sphere has twelve points of contact and forms twelve flat faces. The resultant unit cell is a rhombic dodecahedron shown in Figure 15.

The number of current-paths through the unit cell = 3 .

Therefore, the area of current-flow = $3\pi a^2$ x cos θ,

where θ is the angle between the centre to centre line of spheres in two different planes and the direction of current-flow. The distance between

* Alternative approach in the Appendix
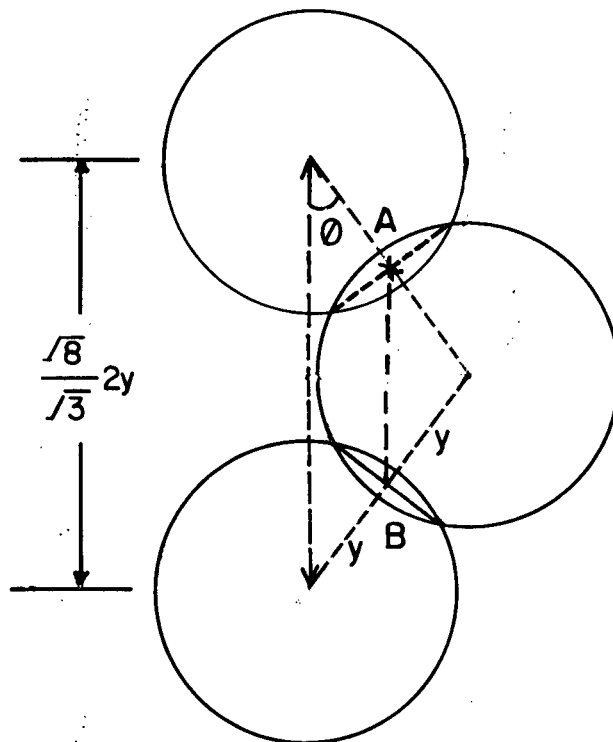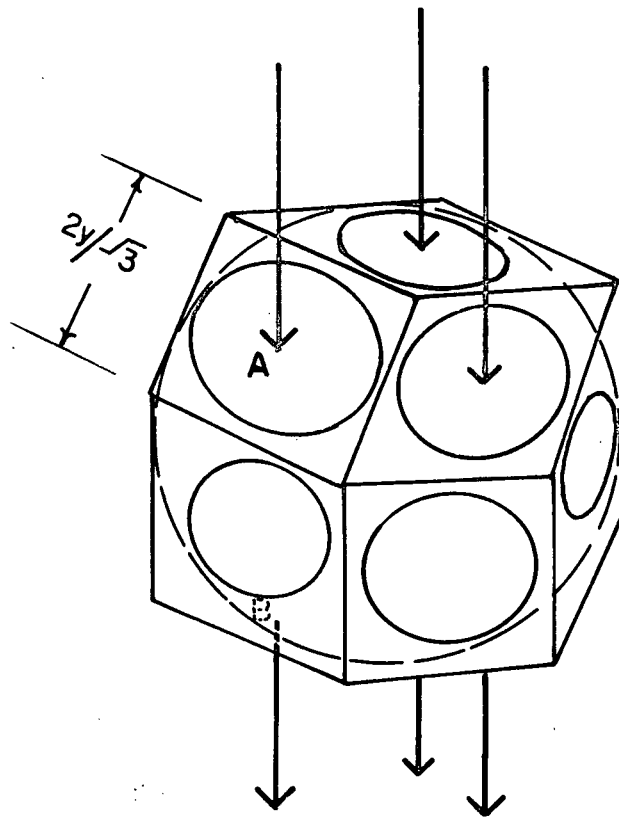
Figure 15. Geometric relationship of rhombohedral model and
current-paths.

centres of any two spheres in contact during deformation = 2y,

and $\cos \theta = \sqrt{2} / \sqrt{3}$, from geometry.

Hence, $A_c = 3\pi a^2 \times \sqrt{2} / \sqrt{3}$.

The length of current-flow through the sphere = $AB = \dfrac{\sqrt{8}}{\sqrt{3}} y = L_c$.

For the unit cell, length of current-flow $= \dfrac{\sqrt{8}}{\sqrt{3}} y = L_s$

Area projected normal to current-flow $= 2\sqrt{3}y^2 = A_s$.

$$\frac{\sigma_m}{\sigma_c} = \frac{L_s}{L_c} \cdot \frac{A_c}{A_s} \qquad \text{(equation 12)}$$

$$= \frac{\dfrac{\sqrt{8}}{\sqrt{3}} y}{\dfrac{\sqrt{8}}{\sqrt{3}} y} \times \frac{\sqrt{6}\ \pi a^2}{2\sqrt{3}\ y^2}$$

i.e.
$$\frac{\sigma_m}{\sigma_c} = \frac{\pi}{\sqrt{2}} \ \frac{a^2}{(R^2 - a^2)} \quad ----------- \quad (15)$$

d) (i) <u>B.C.C. Packing</u>*

The shape of the deformed sphere is schematically represented in Figure 16. There are eight points of contact during the initial stages of deformation.

The number of current-paths = 4.

Area of current-flow = $4\pi a^2 \cos \theta$,

where θ is the angle between centre to centre line of two spheres in contact and the direction of current-flow.

---

* Alternative approach in the Appendix.
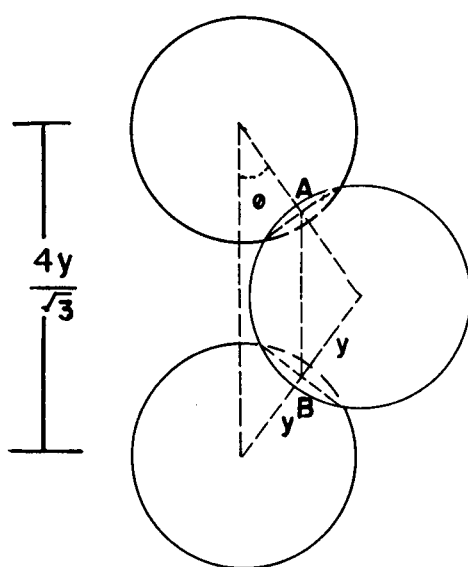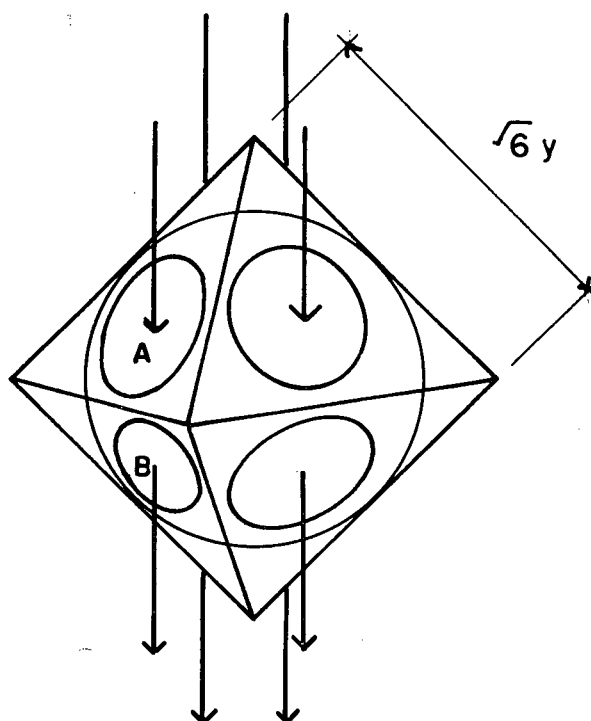
Figure 16. Geometric relationship of b.c.c. model and
current-paths.

$$\cos \theta = \frac{1}{\sqrt{3}} \text{ , from geometry.}$$

$$\therefore \quad A_c = 4\pi a^2 \times \frac{1}{\sqrt{3}} \text{ .}$$

The length of current-flow $\quad = AB = \frac{2y}{\sqrt{3}} \quad y = L_c$.

For the unit cell, $\quad L_s = \frac{2}{\sqrt{3}} y$

Area normal to current-flow $\quad A_s = \frac{16}{3} y^2$.

$$\therefore \quad \frac{\sigma_m}{\sigma_c} = \frac{L_s}{L_c} \cdot \frac{A_c}{A_s} \qquad \text{(equation 12)}$$

$$= 4\pi a^2 \times \frac{1}{\sqrt{3}} \times \frac{3}{16y^2}$$

$$\frac{\sigma_m}{\sigma_c} = \frac{\sqrt{3}}{4} \pi \frac{a^2}{R^2 - a^2} \qquad \text{- - - - - - - (16)}$$

(ii) Tetrakaidecahedron Packing

This is the same as b.c.c. packing, with six additional points of contact giving rise to fourteen flat faces. The unit cell is shown in figure 17. There is an additional current-path through face radius a_2.

Number of current-paths = 4 + 1

Lengths of current-flow are $L_{c_1} = \frac{2}{\sqrt{3}} y_1$ and $L_{c_2} = 2y_2$

where $y_1 = (R^2 - a_1^2)^{1/2}$ and $y_2 = (R^2 - a_2^2)^{1/2}$

$$L_{c_1} = AB = \frac{2}{\sqrt{3}} y_1 \; ; \qquad L_{c_2} = CD = 2y_2$$
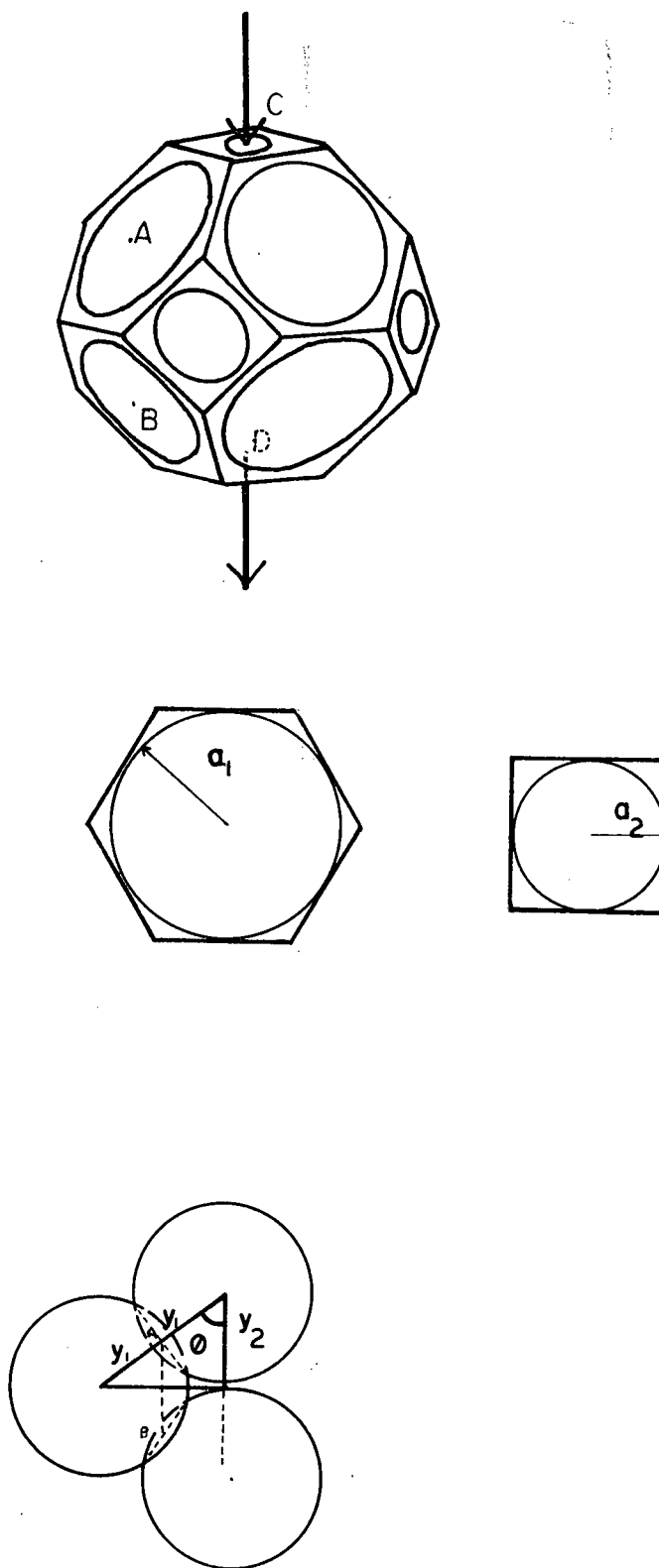
Figure 17. Geometric relationship of tetrakaidecahedron
model and the additional current-path.

Areas of current-flow are $A_{c_1} = 4\pi a_1^2 \times \cos\theta$ and $A_{c_2} = \pi a_2^2$,

where $\cos\theta = \dfrac{1}{\sqrt{3}}$, from geometry.

For the unit cell, $L_{s_1} = \dfrac{2}{\sqrt{3}} y_1$; $L_{s_2} = 2y_2$.

Area of unit cell normal to current-flow is $A_s = \dfrac{16}{3} y_1^2$.

$$\frac{\sigma_m}{\sigma_c} = \frac{L_{s_1}}{L_{c_1}} \cdot \frac{A_{c_1}}{A_s} + \frac{L_{s_2}}{L_{c_2}} \; \frac{A_{c_2}}{A_s}$$

$$= \frac{4\pi a_1^2 \cdot \frac{1}{\sqrt{3}}}{\frac{16}{3} y_1^2} + \frac{\pi a_2^2}{\frac{16}{3} y_1^2} \qquad .$$

Now, $y_1 = \dfrac{\sqrt{3}}{2} y_2$.

Substituting for y_1 and simplifying,

$$\frac{\sigma_m}{\sigma_c} = \frac{\pi}{4} \left[\sqrt{3} \; \frac{a_1^2}{R^2 - a_1^2} + \frac{a_2^2}{R^2 - a_2^2} \right]$$

II.4. DEDUCED RELATIONSHIPS

a) When $R = R_o$

In all four cases, the final form of the equation can be represented by

$$\frac{\sigma_m}{\sigma_c} = \alpha \; \frac{a^2}{R^2 - a^2} \qquad\qquad\qquad - - - - - - - - - - - - - (17)$$

where α is a constant, dependent upon deformation geometry.

The compact density change with respect to contact radius, as given in equation (7), can be modified by using $a = o$ when $D = D_o$, i.e. the initial packing density before deformation. This gives

$$\frac{D}{D_o} = \left[\frac{R_o^2}{R^2 - a^2}\right]^{3/2} \quad \text{-----------} \quad (18)$$

Where R_o is the initial particle radius before deformation. As the deformation proceeds, the value of R increases, as shown by Kakar[26] (Figure 18). It can be seen from the figure that for $a/R < 0.25$, i.e. for small deformations, R remains approximately constant $(R \simeq R_o)$. Then,

$$\frac{D}{D_o} = \left[\frac{R_o^2}{R_o^2 - a^2}\right]^{3/2} \quad \text{-------------} \quad (19)$$

i.e.

$$\left(\frac{D}{D_o}\right)^{2/3} - 1 = \frac{a^2}{R_o^2 - a^2} \quad \text{-------------} \quad (20)$$

Substituting equation (20) in equation (17) we get

$$\frac{\sigma_m}{\sigma_c} = \alpha \left[\left(\frac{D}{D_o}\right)^{2/3} - 1\right] \quad \text{-------------} \quad (21)$$

b) When $R \neq R_o$

A more rigorous derivation, taking into account the variation of R, can be obtained as follows:
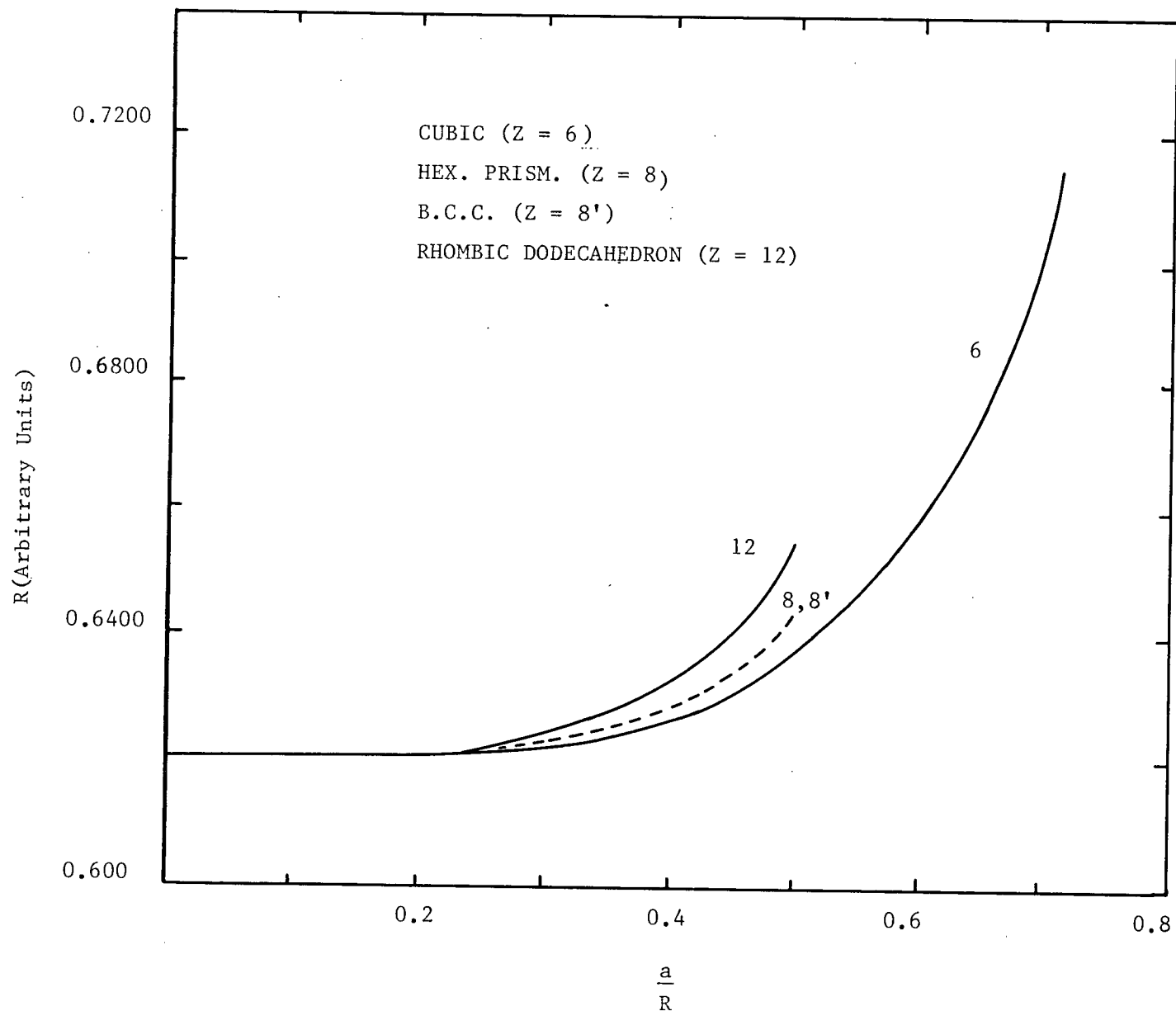
Figure 18. Theoretical relationship of R vs. a/R for the models (After Kakar[26]).

$$D = \frac{1}{\beta(R^2 - a^2)^{3/2}} \qquad \text{(equation 7)}.$$

$$\therefore \quad \beta^{2/3} D^{2/3} = \frac{1}{R^2 - a^2} \quad .$$

Multiplying both sides by R^2, we get

$$D^{2/3} \beta^{2/3} R^2 = \frac{R^2}{R^2 - a^2}$$

$$D^{2/3} \beta^{2/3} R^2 - 1 = \frac{a^2}{R^2 - a^2} \qquad -\, -\, -\, -\, -\, -\, -\, -\, -\, -\, (22)$$

Substituting equation (22) in equation (17) we obtain

$$\frac{\sigma_m}{\sigma_c} = \alpha \left[D^{2/3} \beta^{2/3} R^2 - 1 \right] \qquad -\, -\, -\, -\, -\, -\, -\, -\, (23)$$

The above geometry of deformation is valid only till a critical stage is reached when the flat faces formed on the spheres begin to touch each other. Table II shows the values of α, β, D_o, and (a/R) critical for the different packing geometries. The relative conductivity values for different relative densities have been calculated using the relationship (23) for different packing geometries. The results are plotted in Figure 19. Equations (21) and (23) are the same equation at the initial stages of deformation.
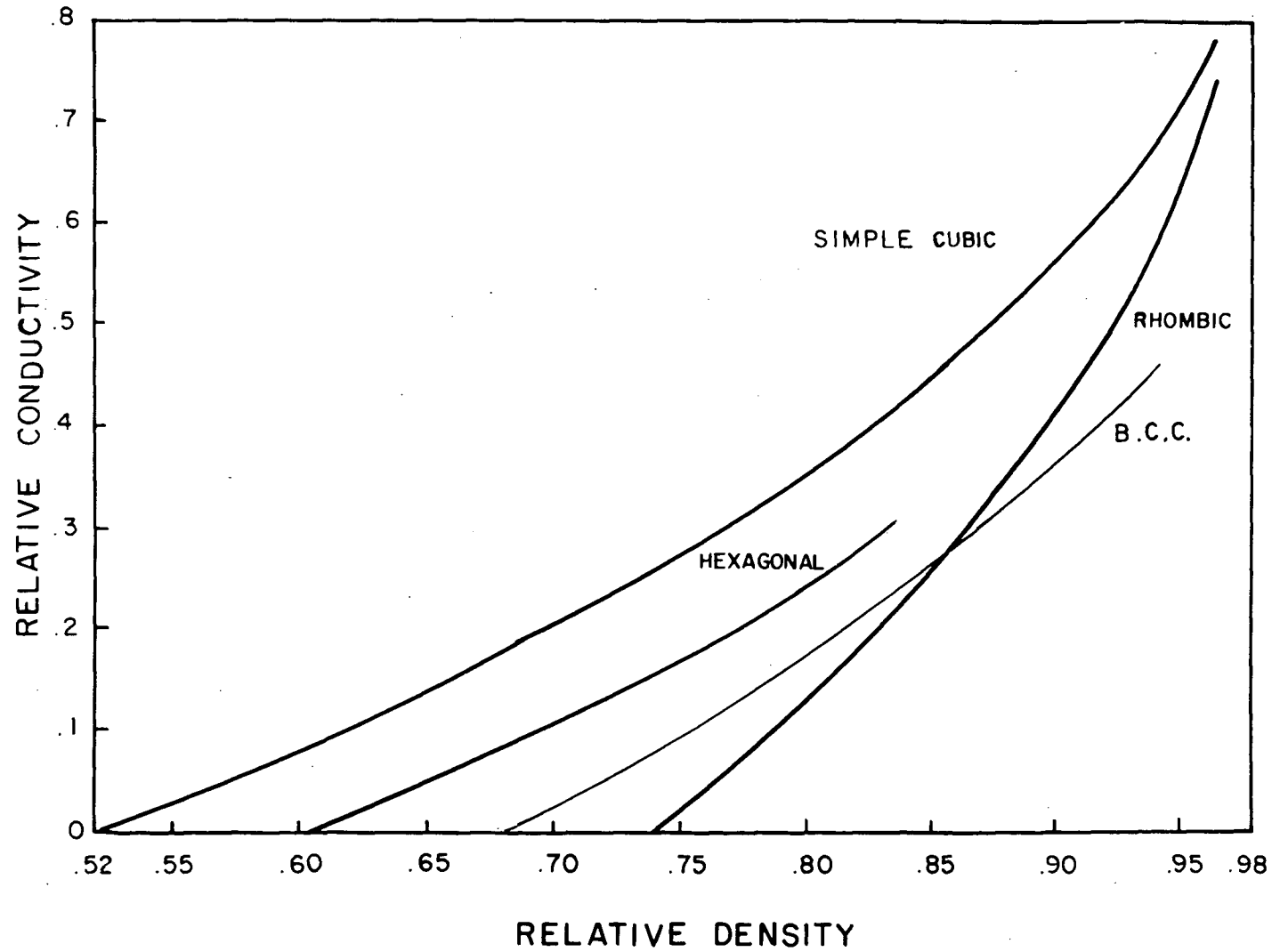
Figure 19. Theoretical relationship of relative conductivity vs. Relative density for the proposed models.

TABLE II

Type of Packing	α	β	D_o in percent	(a/R) Critical
Simple cubic	$\pi/4$	8	52.36	$1/\sqrt{2}$
Orthorhombic	$\pi/2\sqrt{3}$	$4\sqrt{3}$	60.46	$1/2$
Rhombohedral	$\pi/\sqrt{2}$	$4\sqrt{2}$	74.05	$1/2$
b.c.c.	$\pi\sqrt{3}/4$	$32\frac{\sqrt{3}}{9}$	68.02	$1/2$

II.5. PRESENT VS. PREVIOUS CONDUCTIVITY EQUATIONS

Figure 20 shows the theoretical curves of Maxwell[16] and Torkar[19], calculated for spherical pores in a continuous matrix. A value of 0.72, as suggested by Torkar in his paper[19], is used for the structural constant K (equation D Table I). The theoretical curves of the present investigation are superimposed for comparison. The present theory predicts much lower conductivity values for the compacts. This is due to the fact that equation (21) predicts zero conductivity when $D = D_o$, i.e. for the 'green compact'. This need not be so, as discussed in a later chapter. The conductivity σ' of the green compact causes the zero point of the curves to be shifted upwards. Consequently, the theoretical curves lie closer to the Torkar equation. The zero-shift has to be experimentally determined by measuring the conductivity of the green compact, as the relative conductivity of the green compact may vary from almost zero for non-metallic materials to a value between 0.2 to 0.3 for metallic systems.
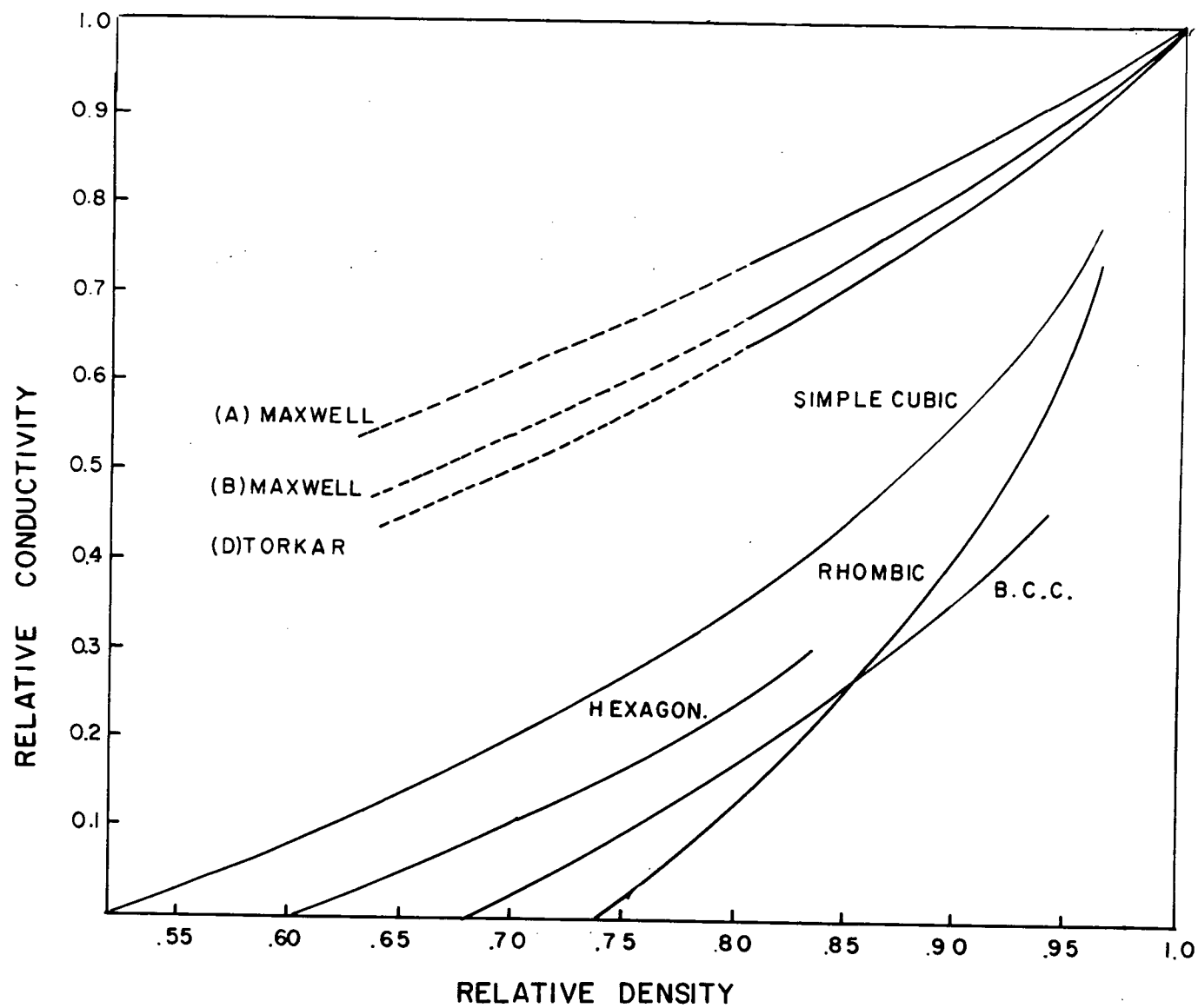
Figure 20. Comparison of the present and previous theoretical equations.

CHAPTER 3

III. EXPERIMENTAL VERIFICATION OF THEORY

To test the theoretical equation (21), it is necessary to determine the electrical resistivity (or conductivity, σ_m) of a compact as a function of relative density. Initial attempts to test the models with porous oxide compacts were not successful, as the resistivity of porous Al_2O_3 or MgO compacts was found to be higher ($>10^{16}$ ohm-cm below $1000^{\circ}C$) than any die materials that can be used for hot-pressing. For this reason, the models are tested with spheres of soda-lime-silica glass, having a resistivity between 10^4 to 10^2 ohm-cm in the temperature range 550 to $650^{\circ}C$. The glass spheres used are of two sizes - 0.70 mm and 0.42 mm average diameter (Figure 21, a & b), the nominal composition of which is SiO_2 70%, Al_2O_3 2%, CaO 12%, MgO 2%, and Na_2O 10%. The glass spheres were supplied by the 3 M company, St. Paul, Minnesota.

The model is also tested on nickel spheres of 0.65 mm average diameter (Figure 21c), supplied by the Sherritt Gordon and Company, Fort Saskatchewan, Alberta.

III.1. EQUIPMENT

It was necessary to measure the conductivity of glass at a sufficiently elevated temperature ($550 - 650^{\circ}C$), as the room temperature conductivity was greater than 10^{15} ohm^{-1}-cm^{-1}. The equipment was built to measure the conductivity and the bulk density of the glass compacts simultaneously during hot-pressing. A schematic diagram of the equipment is shown in Figure 22. Stainless steel plungers were used as electrodes. Small sections of transparent silica glass tubing of 17 mm diameter were used as the die material, as silica glass has a very high
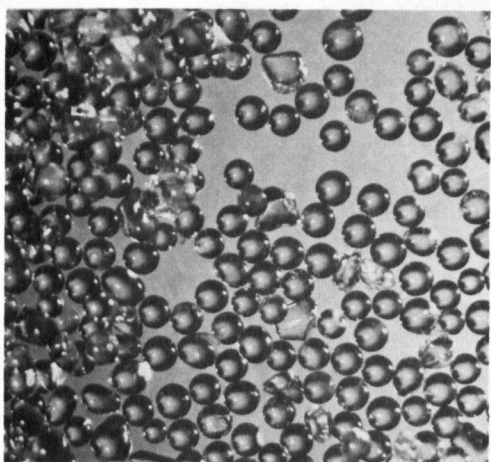
(a)
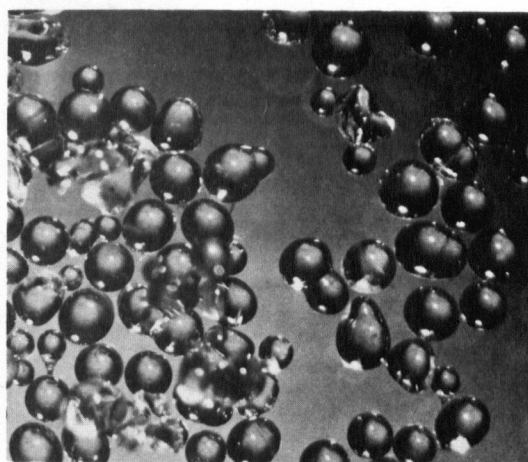
(b)
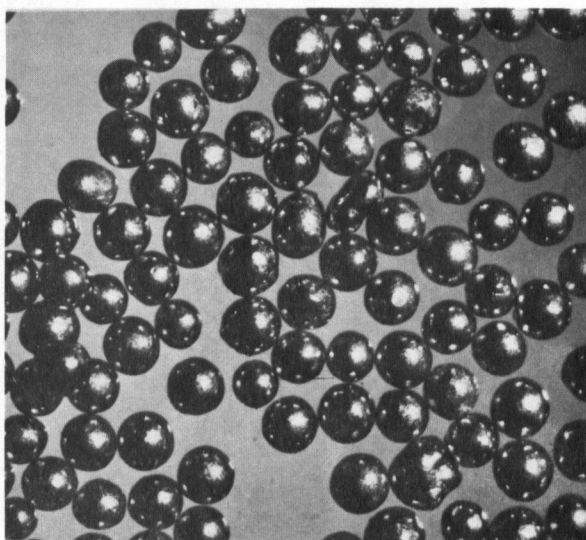
(c)

Figure 21. Photographs of a) glass spheres, 0.42 mm average dia.,
                          b) glass spheres, 0.70 mm average dia.,
                          c) nickel spheres, 0.65 mm average dia.

Magnification x 10.
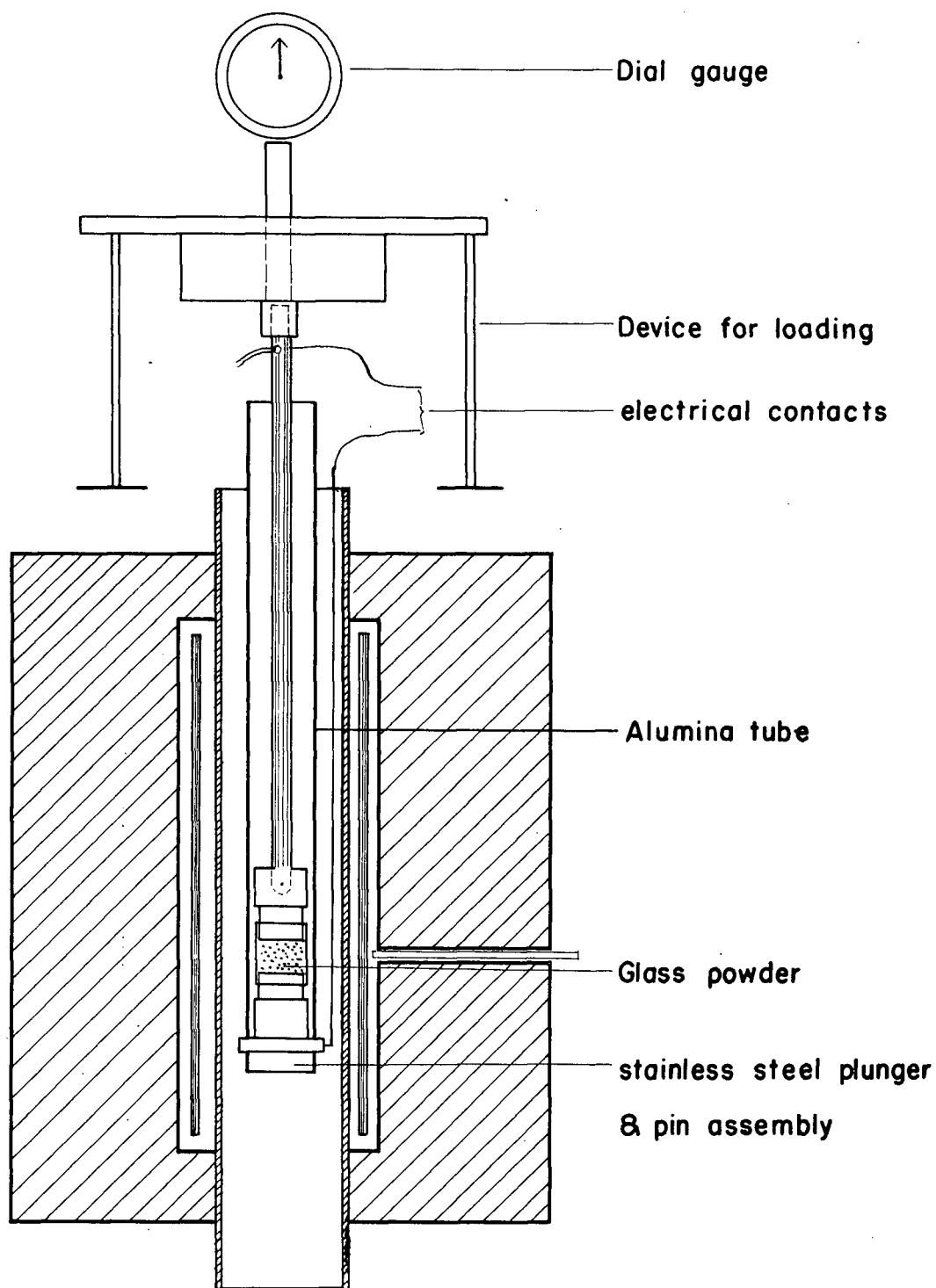
Figure 22. Schematic diagram of the equipment used for
resistivity measurements of glass spheres.

electrical resistivity below 700°C (>10^{16} ohm-cm). The die and the electrodes were inserted into a recrystallised alumina tube and held by a stainless steel pin, which also served as an electrical lead. The alumina tube was lowered into the furnace. Shrinkage was measured with a dial gauge having a sensitivity of 0.0002" per division. This gauge was mounted on the alumina tube with its pin resting on a porcelain rod fitted into the upper electrode.

Electrical resistance was measured with an Impedance bridge (range 10^{-3} to 10^{7} ohms), operated at 1K c/s and 6v. A simple loading device, made up of a lever arm and pans, was used, as indicated in the figure. A maximum of 25 lbs. could be loaded on the pans, which was sufficient to hot-press the glass compacts to a pressure of 50 p.s.i., in the temperature range 550 - 650°C.

III.2. PROCEDURE

The glass spheres were cleaned with dilute hydrofluoric acid, washed and dried with isopropyl alcohol to eliminate adsorbed water. A weighed amount of the glass spheres was loaded into the die, tapped and well-shaken in order to obtain a uniform packing. The as-compacted density was calculated from the initial volume of the compact and true density of the glass which was determined by the pycnometric method. It took 20 to 25 minutes for the specimen to reach the furnace temperature, after the assembly was introduced into the furnace. During this heating - up period no appreciable shrinkage was recorded on the dial gauge. The experiments were carried out in dry air, as presence of water vapour and low partial pressures of oxygen have been known to affect the electrical conductivity of glass.[28] A.C. resistivity was measured in

preference to D.C. to avoid electrode polarization, as glass is usually

an ionic conductor. A calibration experiment was initially performed

(without the glass spheres) to standardize the shrinkage curves.

III.3. MEASUREMENT ON NON-POROUS GLASS

In order to test equation (21), it was necessary to know

the conductivity of the non-porous glass. For this, the following

procedure was adopted: a batch of glass spheres was melted in a

platinum crucible at 1500°C and held at this temperature for 24 hours

to eliminate pores. After 24 hours, the crucible was rapidly withdrawn

from the furnace. The glass was cast into pre-heated stainless steel

moulds. It was annealed in air at 600°C for eight hours and furnace

cooled. Thin specimens of 17 mm diameter and 5 mm thick were cut with

an ultrasonic vibrator and silicon carbide suspension in petroleum

liquid. Both faces of the specimens were ground flat and as parallel as possible

to each other on the diamond-polisher. To ensure good electrical contact

with the electrodes, gold was vapour deposited on the faces of the glass

with a guard-ring on one side. The purpose of this guard-ring is to

prevent surface leakage. The glass specimen was equilibrated at different

temperatures for different periods, for the conductivity determination.

III.4. PROCEDURE FOR NICKEL SPHERES

The nickel spheres were initially cleaned and then held in

a stream of cracked ammonia at 650°C for 4 hours to reduce surface oxide.

The hot-pressing was carried out in a Philips 12 KW induction unit.

An ½" Inconel die with a graphite sleeve and Inconel plungers were used

for hot-pressing (Figure 23). A weighed amount of spheres was tapped

into the die,with graphite spacers between the spheres and the rams to

prevent adherence between nickel and the Inconel. The die and plunger

assembly was mounted on a hydraulic press and enclosed in a quartz

tube. An inert atmosphere was maintained around the die during

hot-pressing which was carried out under 7200 p.s.i. and at $800^{o}C$. The

shrinkage was measured with a dial gauge. The sample was cooled to

room temperature in the die and them removed. The apparent density

was determined from the weight to volume ratio. True density was

determined by the pycnometric method. Specimens of different relative

densities were produced following the above procedure.

D.C. conductivity for the hot-pressed specimens was measured

at room temperature using a Kelvin bridge (Pye Cat.no. 7415). As the

change in electrical resistivity of nickel compacts is in the order of

several micro-ohms, the following procedure was adopted.

The compact was mounted inside a vise made of lucite. A

steady current of 7 amps. was passed through the compact. To obtain

uniform current distribution across the cross-sectional area, thin

lead discs (reagent grade) were pressed against the sides of the compact;

the current terminals were held against the lead discs by screws

provided on either side of the vise. Two potential probes were introduced

as shown in Figure 24 at a fixed distance apart. The probes were

made of nickel (to eliminate contact potentials with the specimen). Their

ends were narrowed to small hemispherical tips to ensure good electrical

contact. The nickel probes were set in two reamed holes to prevent any
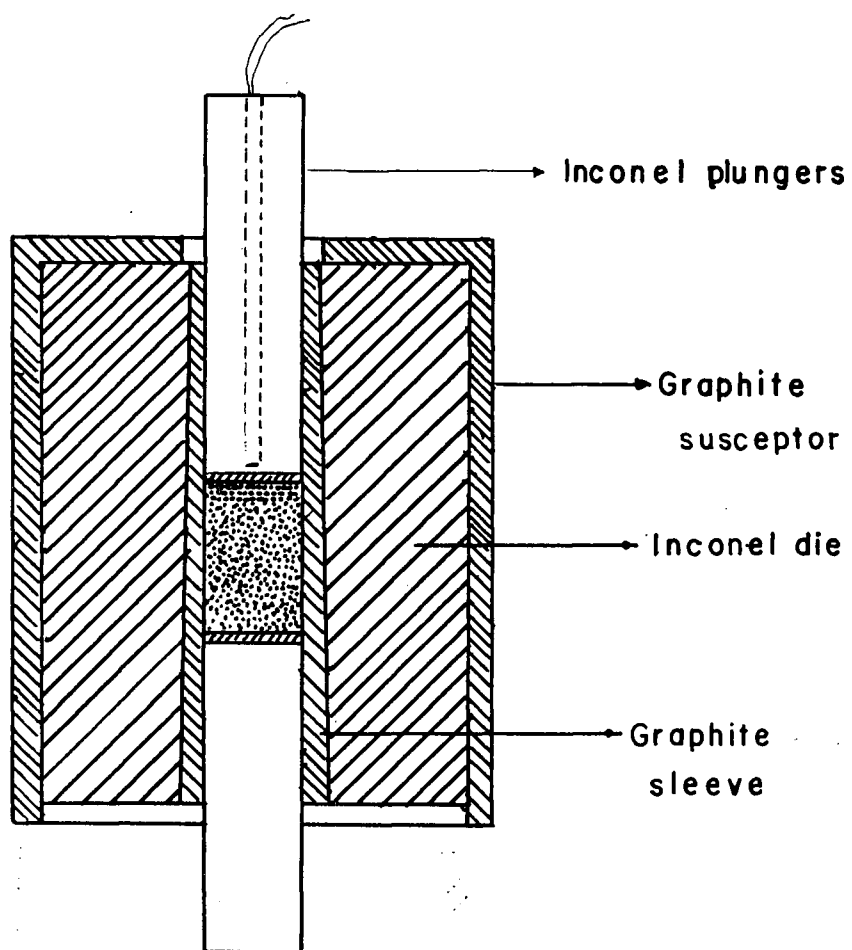
Figure 23. Schematic diagram of the die used for hot-pressing
nickel spheres.
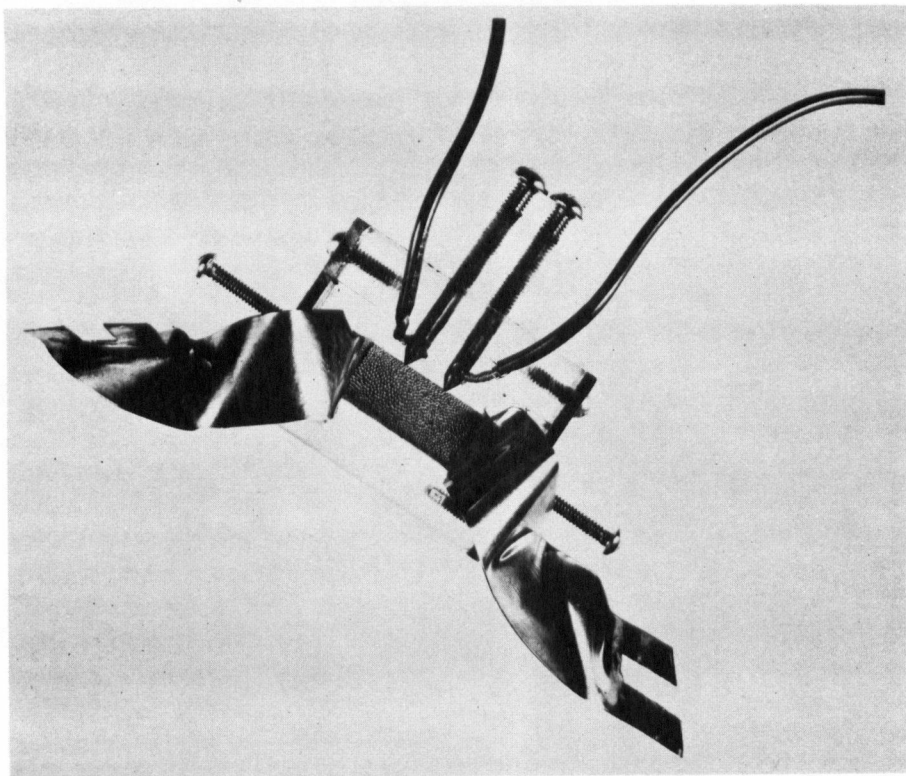
Figure 24. Photograph of the vise used to measure the
electrical conductivity of nickel compacts.

sideways movement. A number of measurements were made using the Kelvin bridge and a deflection galvanometer (Tinsley Type S.R. 4/45). It was observed that any variation in the pressure of the probes against the specimen produced insignificant changes in the readings. The electrical conductivity was calculated for each specimen from the measured resistance values.

CHAPTER 4

IV. RESULTS AND DISCUSSION

IV.1. CONDUCTIVITY VS. DENSITY FOR GLASS

The electrical resistivity of the compacts of glass spheres was measured continuously as a function of density during hot-pressing under isothermal conditions. The volume of the compact was calculated using the height of the compact at any stage of densification (indicated by the dial gauge) and the diameter of the die, which remained constant. The electrical conductivity σ_m, was calculated from the resistance measurements. The σ_m values are plotted as a function of relative density for three different temperatures as shown in Figure 25a and b. The conductivity of the compact increased with increase in relative density.

IV.2. CONDUCTIVITY VS. RELATIVE DENSITY FOR NICKEL

Compacts of nickel spheres were hot-pressed at 800°C under a pressure of 7200 p.s.i. for differing periods to obtain different relative densities. These compacts were subsequently used for D.C. conductivity measurements at room temperature. The results are plotted as a function of relative density, as shown in Figure 26.

IV.3. TEST OF THEORETICAL MODELS

The theoretical models were tested by comparing the results with the general equation

$$\frac{\sigma_m}{\sigma_c} = \alpha\left[\left(\frac{D}{D_o}\right)^{2/3} - 1\right] \qquad - - - - - - - - (21)$$
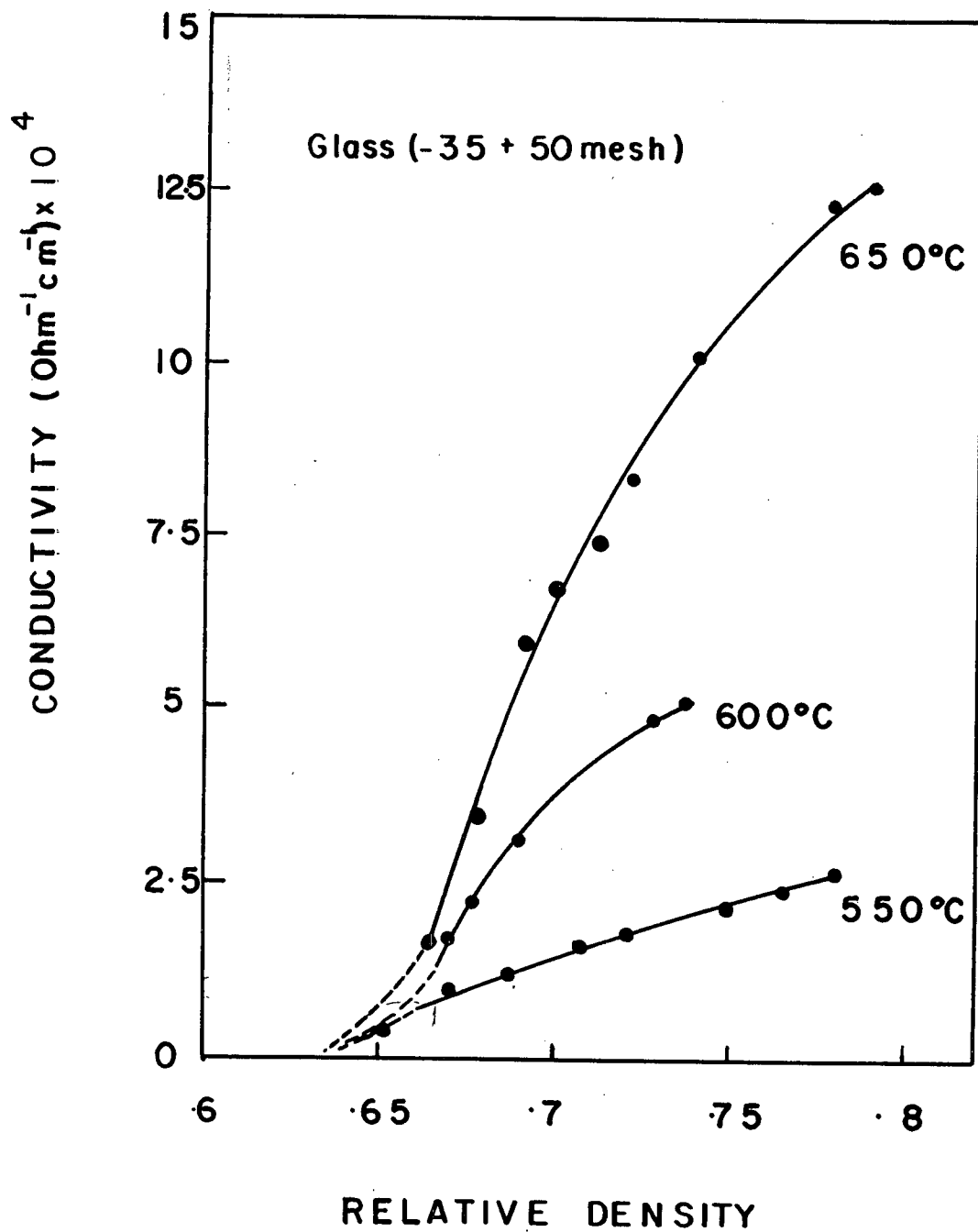
Figure 25.a. Conductivity vs. Relative density for glass compacts at different temperatures.
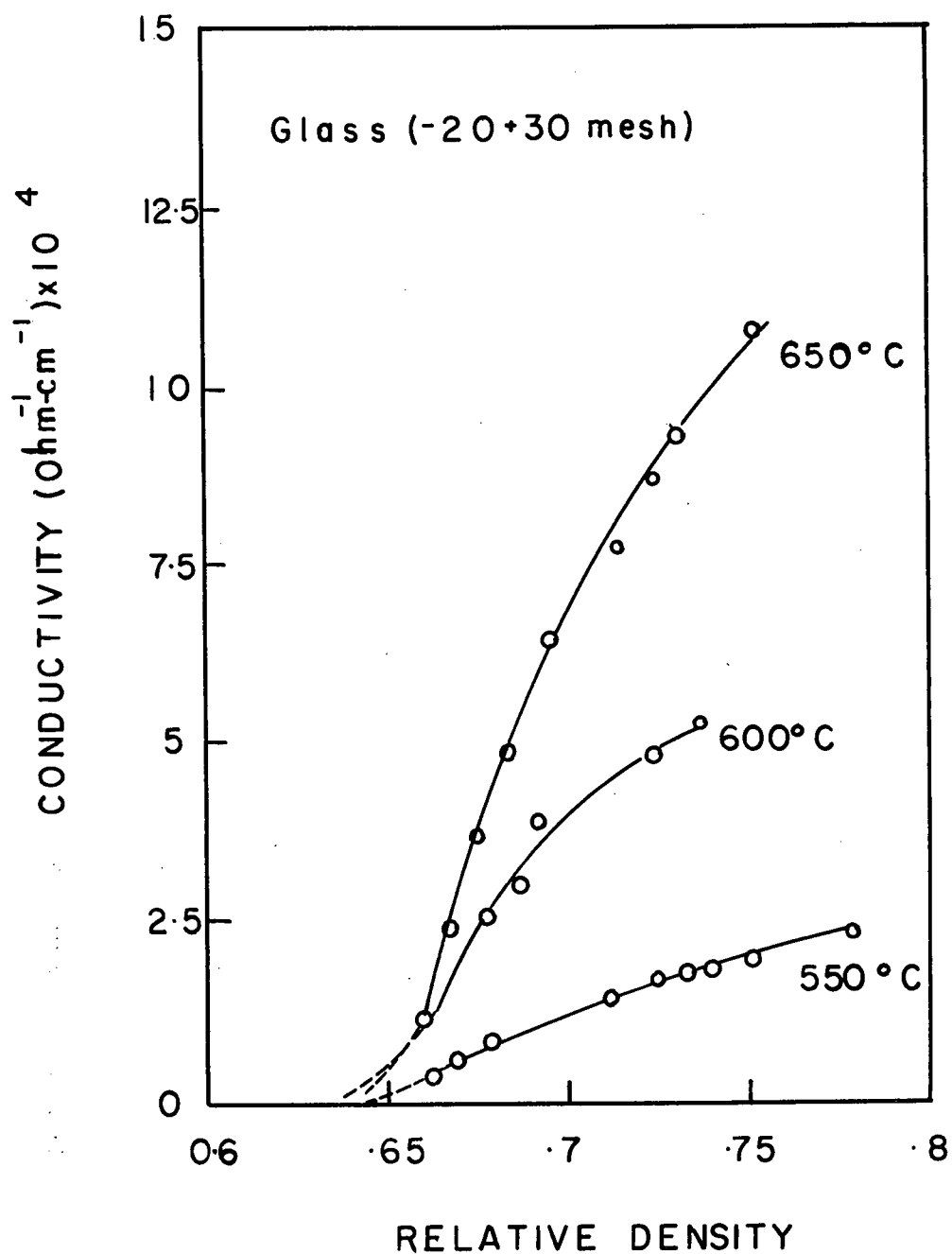
Figure 25.b. Conductivity vs. Relative density for glass compacts at different temperatures.
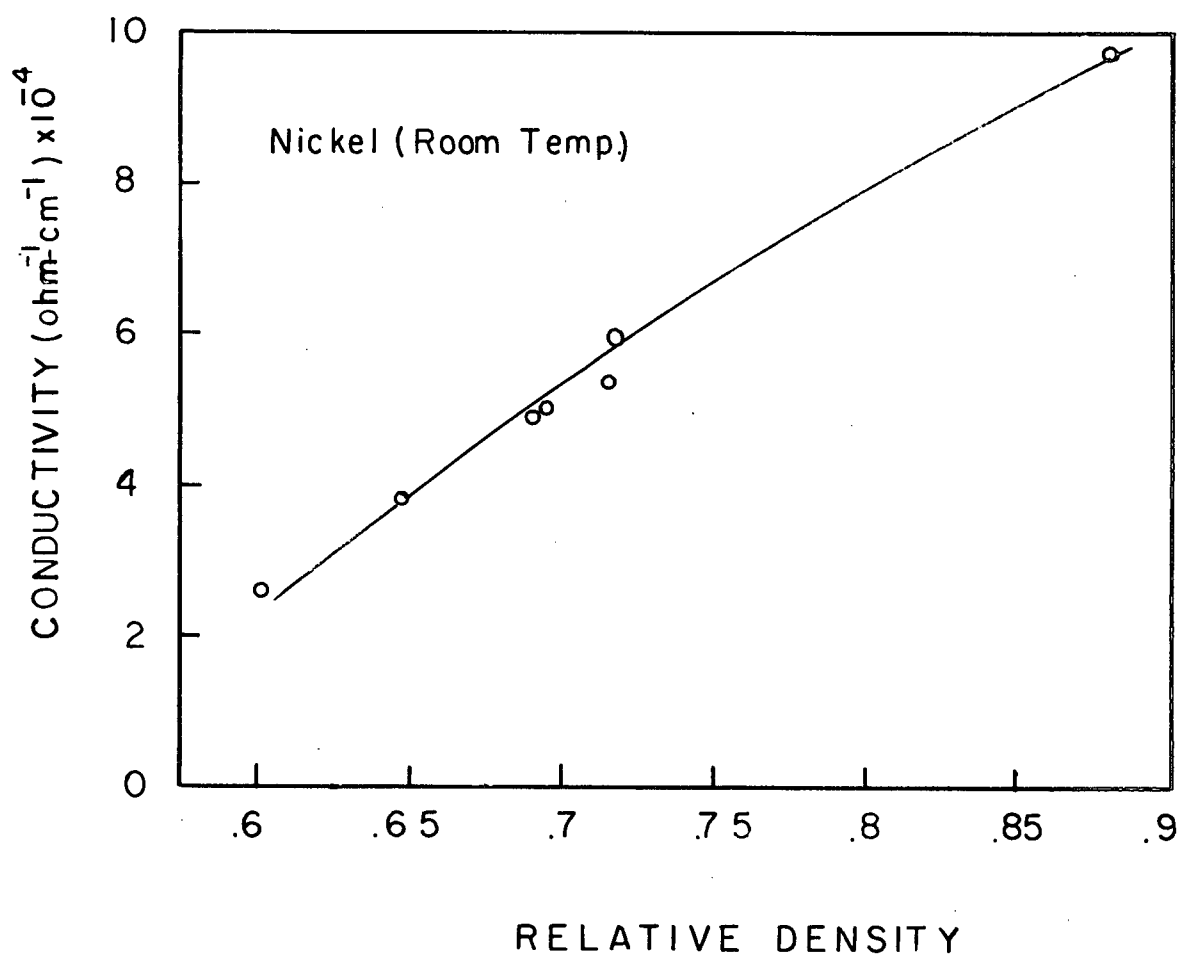
Figure 26. Conductivity vs. Relative density for nickel compacts at room temperature.

Where σ_m and D are experimentally measured variables;

σ_c = a material constant and α = a geometric constant.

D_o is the initial bulk density, which is constant for a given experiment.
Hence, log σ_m is plotted vs. $\log\left[\left(\dfrac{D}{D_o}\right)^{2/3} - 1\right]$ in Figure 27, which
shows that at every temperature the plot is linear with a slope close
to unity for most of the data. This agreement between the theoretical
prediction and the experimental data confirms the validity of the above
equation. The deviation from the predicted curve, in the initial stages
of densification, is due to particle rearrangement in the density range
60 to 66%. The density increase in this range is caused by particle
sliding as well as by plastic deformation, rather than by plastic
deformation alone. This particle sliding changes the coordination
number and establishes a greater number of current paths. Beyond 66%,
the density increases mostly by neck growth at the points of contact
and the theoretical equation is obeyed.

IV.4. ELECTRICAL CONDUCTIVITY OF GLASS

As the temparature is raised, the conductivity of solid
glass rapidly increases and over a considerable temperature range, the
conductivity can be represented by an Arrhenius type of equation,

$$\sigma = \sigma_o \, e^{-Q/RT}$$

where σ_o = a temperature independent constant

Q = experimental activation energy for conduction.

R and T have their usual meanings.

Terai[29] has pointed out that in sodium aluminosilicate
glasses of composition similar to that used in this study, the electrical
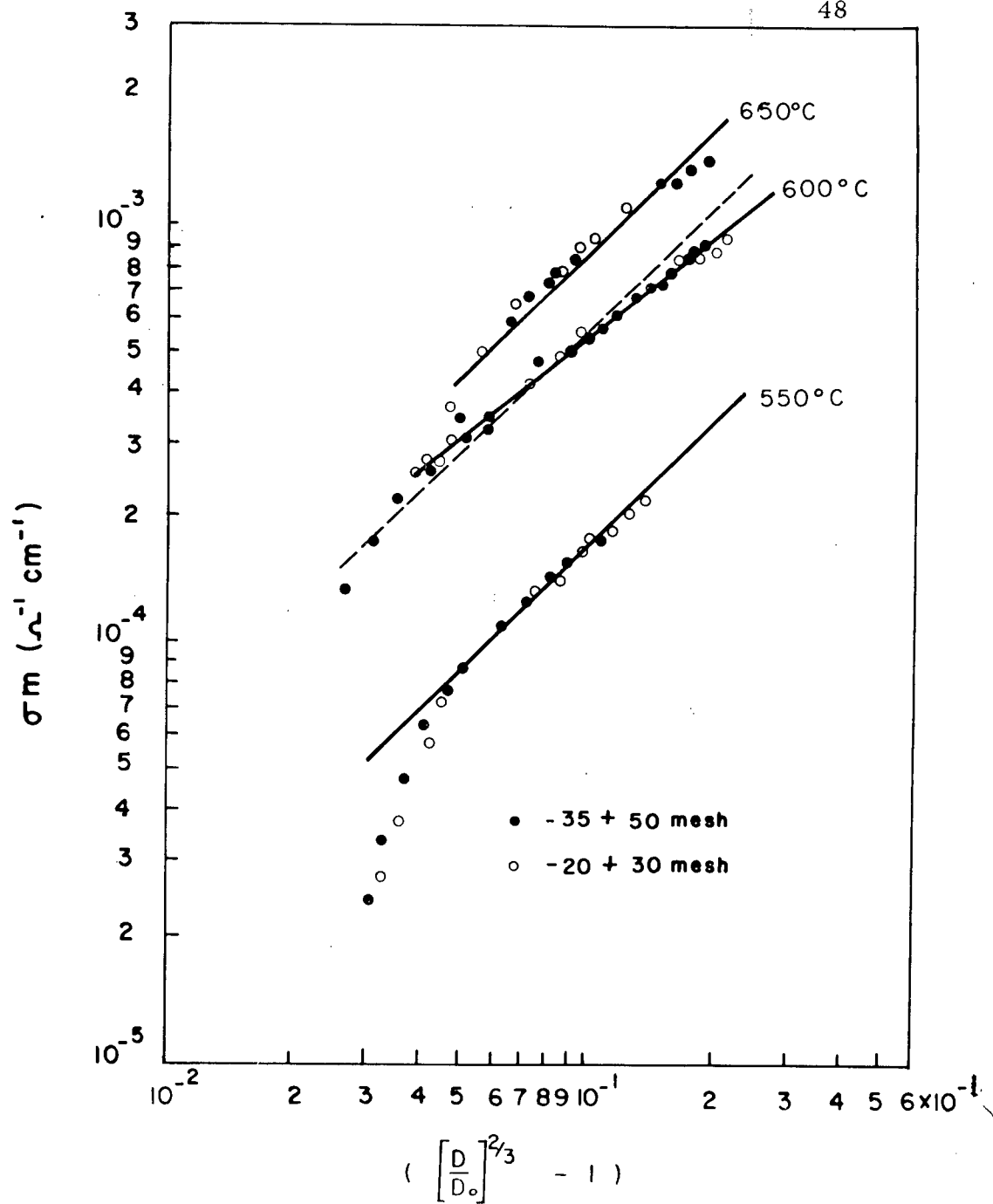
Figure 27. Log σ_m vs. $\log\left[\left(\dfrac{D}{D_o}\right)^{2/3} - 1\right]$ for glass compacts.

conductivity is electrolytic. The current is mainly carried by the sodium-ions moving through the 'holes' in the structure, and the transport number of sodium ions is close to unity for sodium aluminosilicate glasses.

To study the temperature dependence of electrical conductivity, the logarithm of the conductivity of the non-porous glass is plotted against the reciprocal of absolute temperature in Figure 28. The conductivity of a glass reaches an equilibrium value at a given temperature only after a long interval of time (Kaneko and Isard[30]). However, the conductivity values measured in this work after a fixed time interval at different temperatures, lie on a straight line. Figure 28 shows that the log conductivity vs. 1/T relationships after constant intervals have nearly the same slope. In order to measure the equilibrium conductivity at $600^{\circ}C$, the specimen was held for 72 hours at this temperature till it attained a steady value, which was 3.5×10^{-3} ohm^{-1} cm^{-1}. This value is now substituted for σ_c in equation (21). Thus the only unknown parameter α in equation (21) can be calculated. The value of α was found to be 0.9.

Equation (21) can be rewritten as,

$$\log \sigma_c = \log \sigma_m - \log \alpha - \log \left[\left(\frac{D}{D_o} \right)^{2/3} - 1 \right] \quad ----(24)$$

Using $\alpha = 0.9$ and equation (24), log σ_c values at different temperatures were calculated and plotted in Figure 29. This figure also includes the logarithmic conductivity values for a porous glass
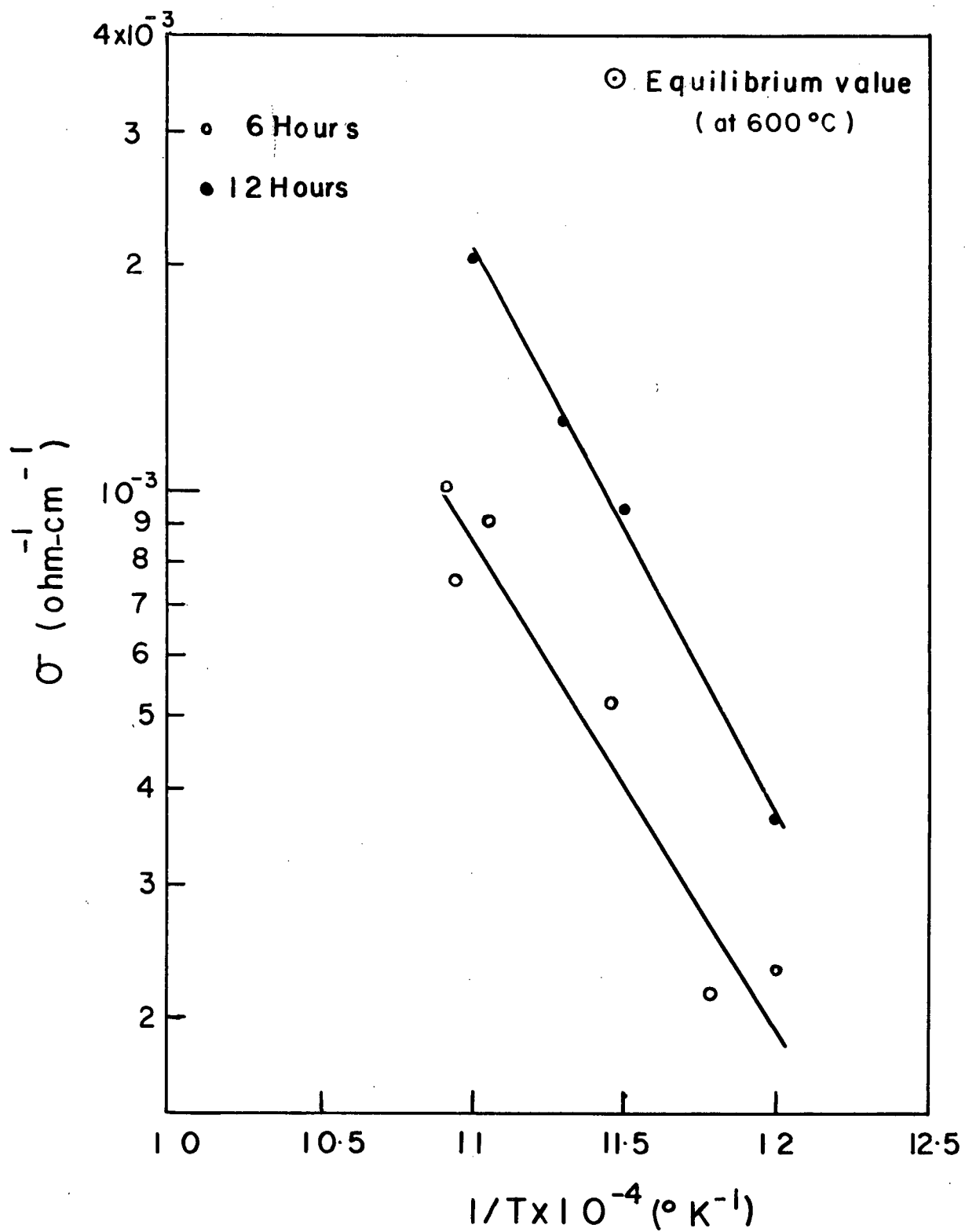
Figure 28. Log σ vs. $\frac{1}{T}$ for the non-porous glass at different times.
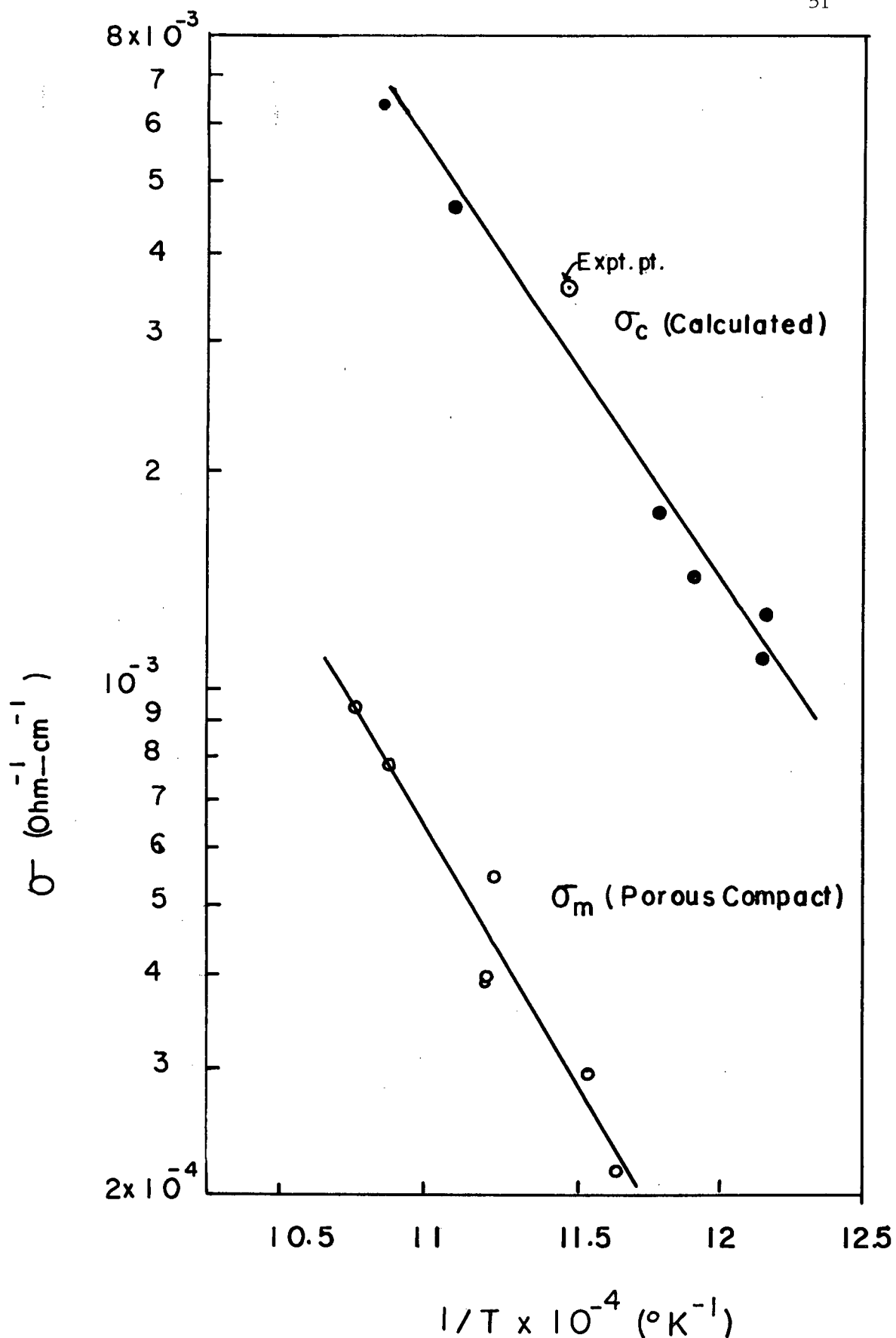
Figure 29. Log σ_c (calculated) vs. $\frac{1}{T}$ for non-porous glass and log σ_m vs. $\frac{1}{T}$ for porous glass.

(relative density = 0.7). For the porous glass, equation (21) can be rewritten, replacing σ_c by $\sigma_o \, e^{-Q/RT}$:

$$\sigma_m = \alpha \, \sigma_o \left[\left(\frac{D}{D_o} \right)^{2/3} - 1 \right] e^{-Q/RT}$$

At a constant relative density, log σ_m vs. $1/T$ gives the experimental activation energy for porous glass, which has been found to be the same as for the non-porous glass.

The lines in Figures 28 and 29 have a slope of $(0.67 \pm .05) \times 10^{-4}$ degrees Kelvin and the corresponding activation energy for electrical conductivity is 30 ± 3 kcal/mole. This value is similar to the values reported in literature (25 to 30 kcal/mole) for sodium-aluminosilicate glasses.

IV.5. RELATIVE CONDUCTIVITY VS. RELATIVE DENSITY

Figure 30 shows the plot of relative conductivity vs. relative density for glass spheres of two different sizes at 550°C. The calculated σ_c values from Figure 29 were used for calculating the relative conductivity (σ_m/σ_c) at different temperatures. The relative conductivity values follow the general trend of the theoretical curves, which are superimposed in the figure for comparison. Figures 31 and 32 show similar plots for the results obtained at 600°C and 650°C. The deviation in the range .60 to .66 relative density is again indicative of the contribution from particle rearrangement.

IV.6. ELECTRICAL CONDUCTIVITY OF THE 'GREEN COMPACT'

The theoretically derived equation (21) has the boundary condition that when $D = D_o$, $\sigma_m = o$, i.e. the electrical conductivity of
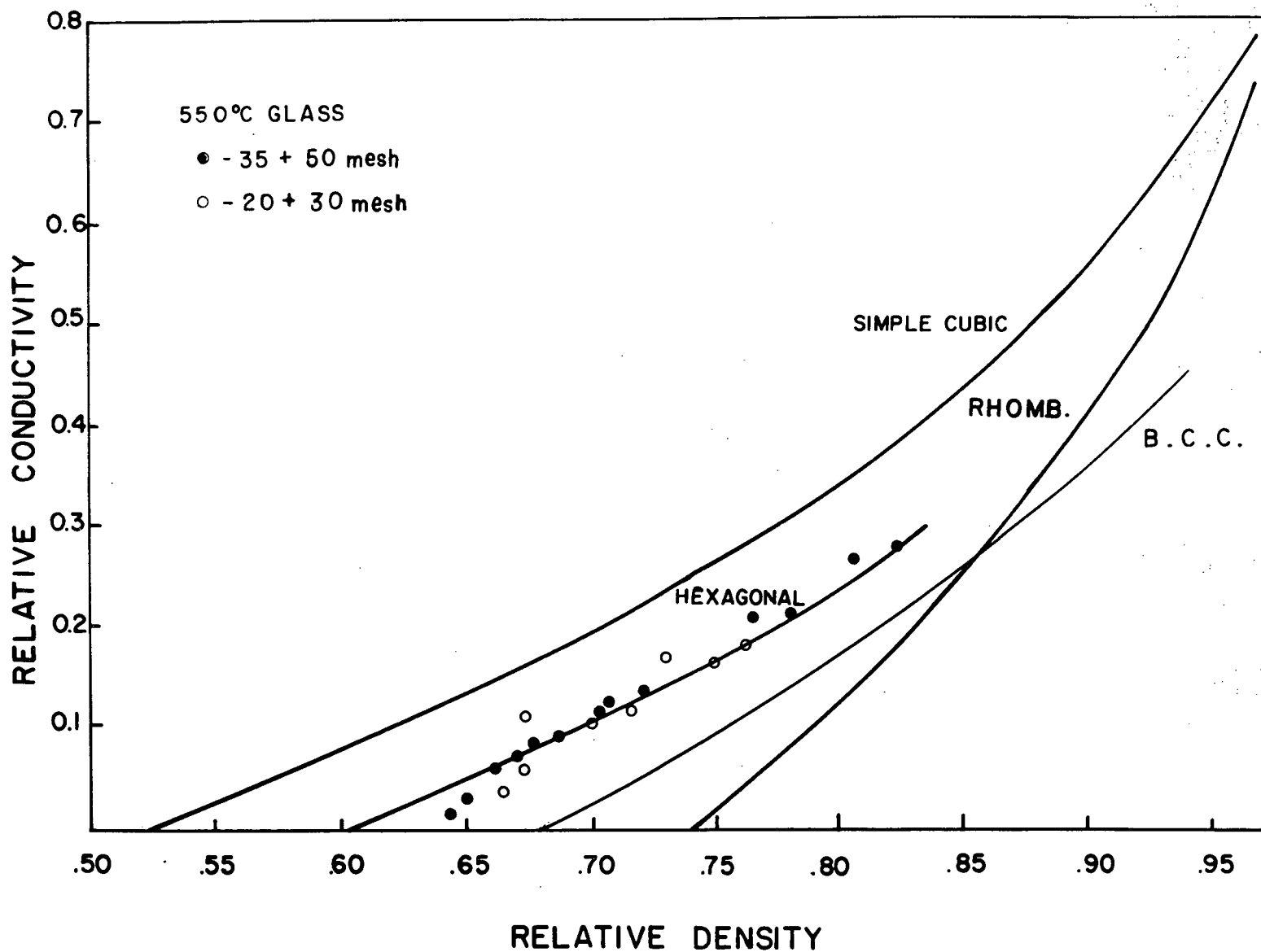
Figure 30. Relative conductivity vs. relative density for glass at 550°C.
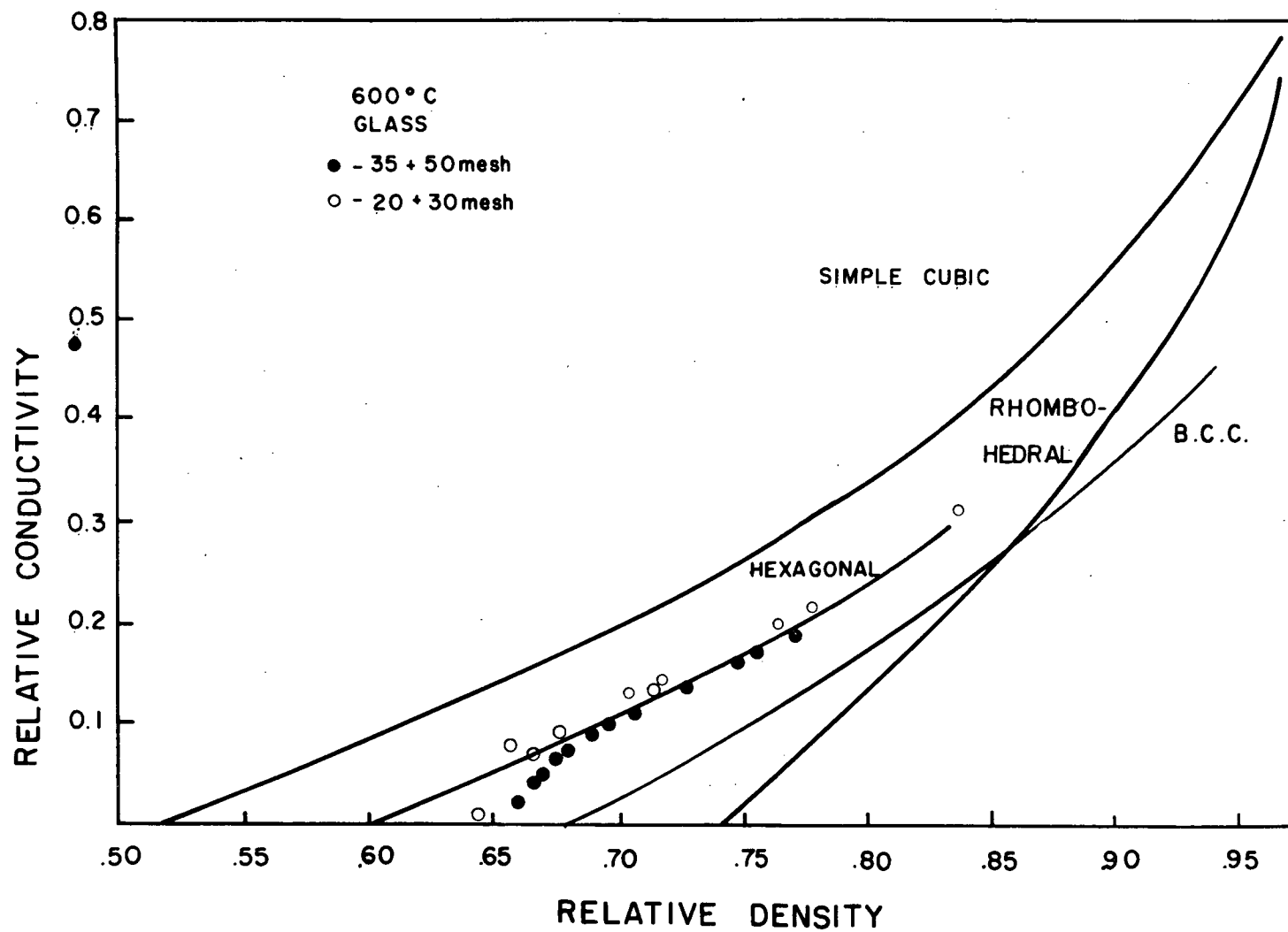
Figure 31. Relative conductivity vs. Relative density for glass at 600°C.
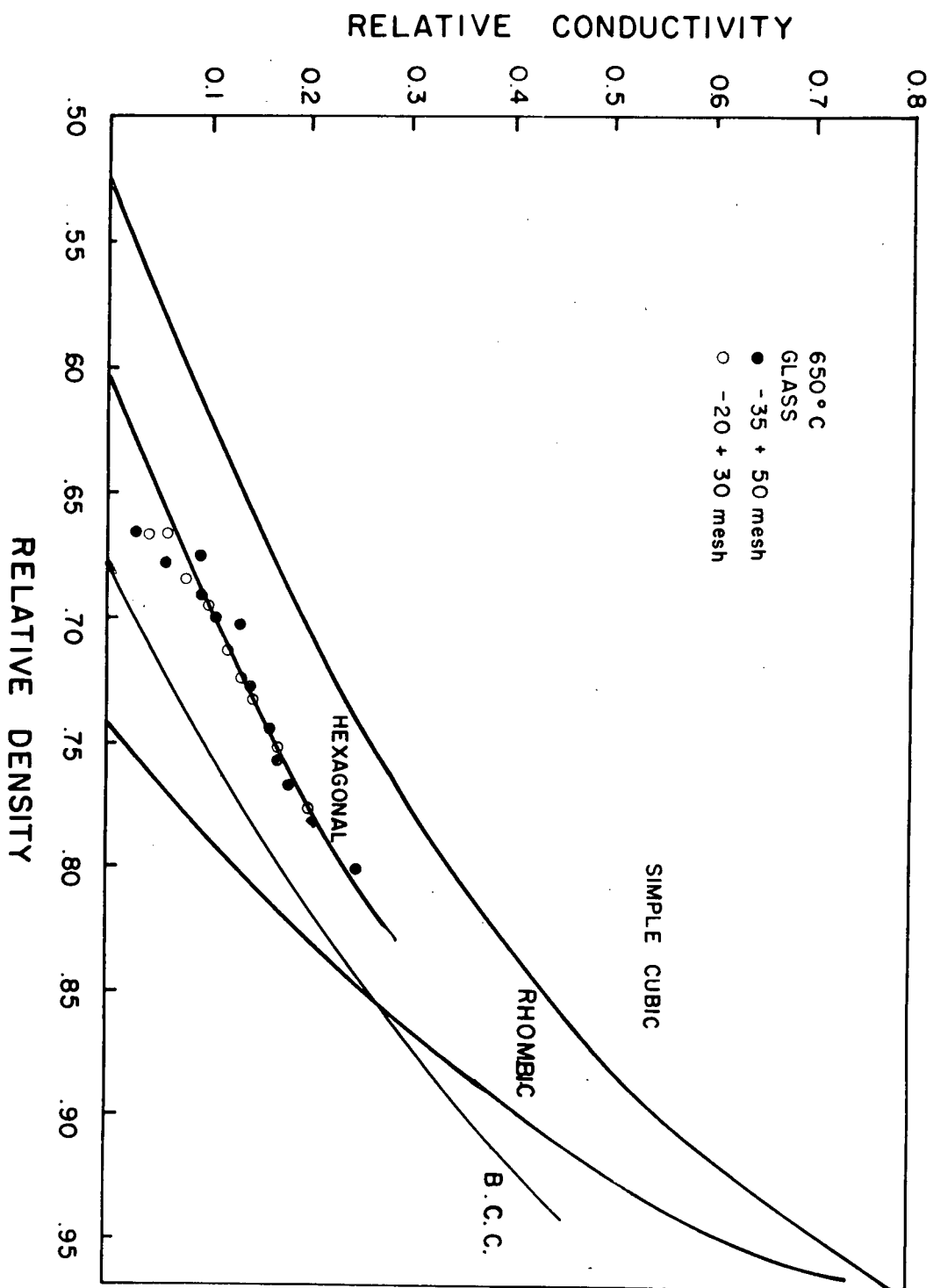
Figure 32. Relative conductivity vs. Relative density for glass at 650°C.

the compact before deformation is zero. However, the particles in

contact with each other, before hot-pressing, do have a certain

conductivity. As a result equation(21) should be modified as

$$\sigma_m = \sigma' + \alpha\sigma_c \left[\left(\frac{D}{D_o}\right)^{2/3} - 1 \right] \text{ --------- (25)}$$

where σ' is the electrical conductivity of the compact before deformation.

Equation(25) can be rewritten as,

$$\left[\frac{\sigma_m}{\sigma_c} - \frac{\sigma'}{\sigma_c} \right] = \alpha \left[\left(\frac{D}{D_o}\right)^{2/3} - 1 \right] \text{ --------- (26)}$$

Thus, the experimental results have to be corrected for a zero-error

along the ordinate. For glass this error is negligible, as the relative

conductivity of the green compact, $\frac{\sigma'}{\sigma_c}$ is < .005, below .63 relative

density.

The results for compacts of nickel spheres demonstrate the

effect, when σ'/σ_c is rather large (Figure 33). The relative

conductivity of the green compact (.60 relative density) was found to

be 0.18. The results were corrected for this error and replotted in

Figure 34. This corrected data fit the theoretical models more closely.

IV.7. VERIFICATION OF THEORETICAL MODELS WITH PREVIOUS RESISTIVITY DATA

As discussed previously, a large amount of data are available

on the resistivity of metal powder compacts. Although most of these

compacts were made-up of random-shaped particles, it would be interesting

to see if any of these data fit the equation derived in this work. In
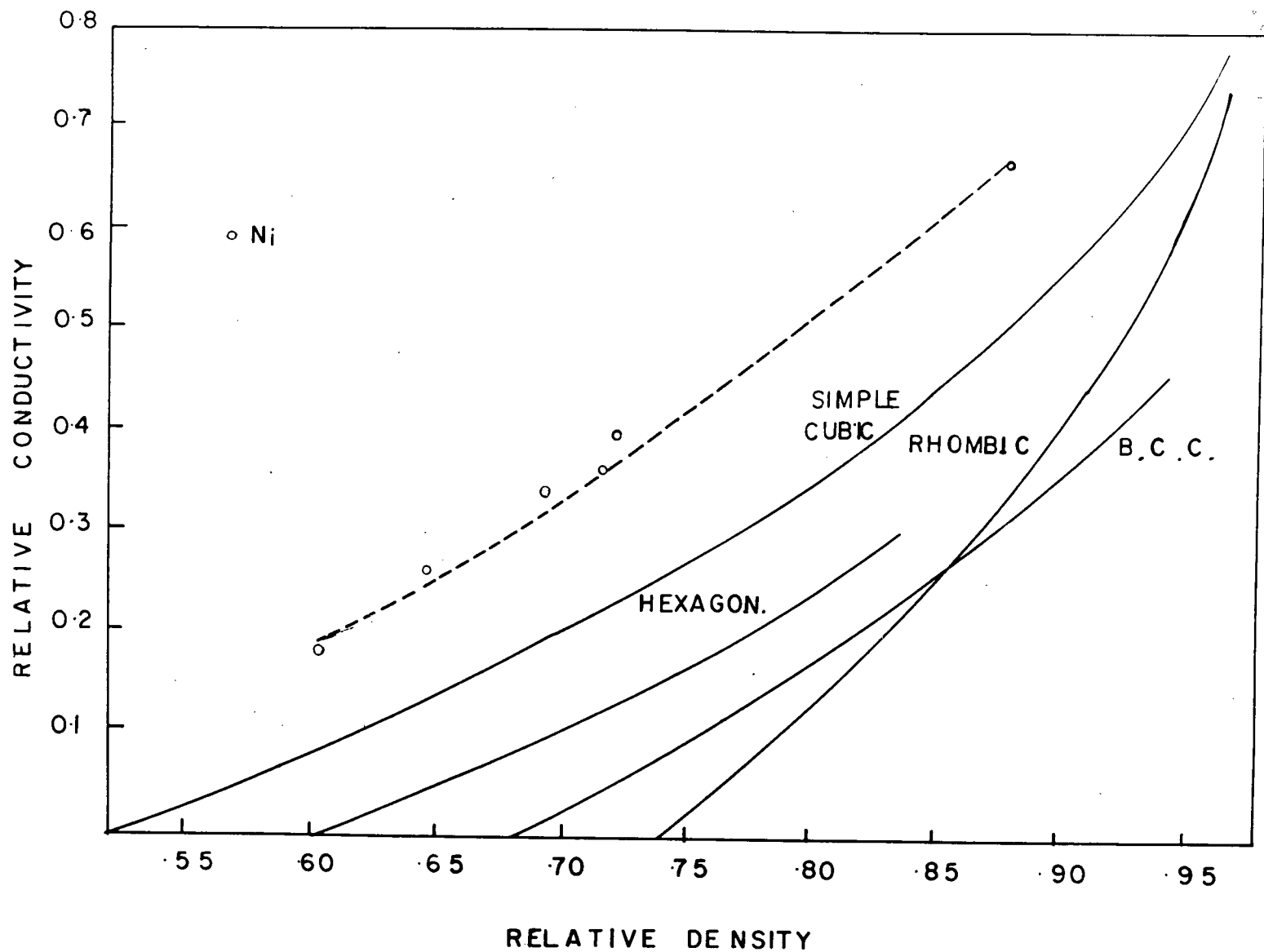
Figure 33. Relative conductivity vs. Relative density for nickel at room temperature.
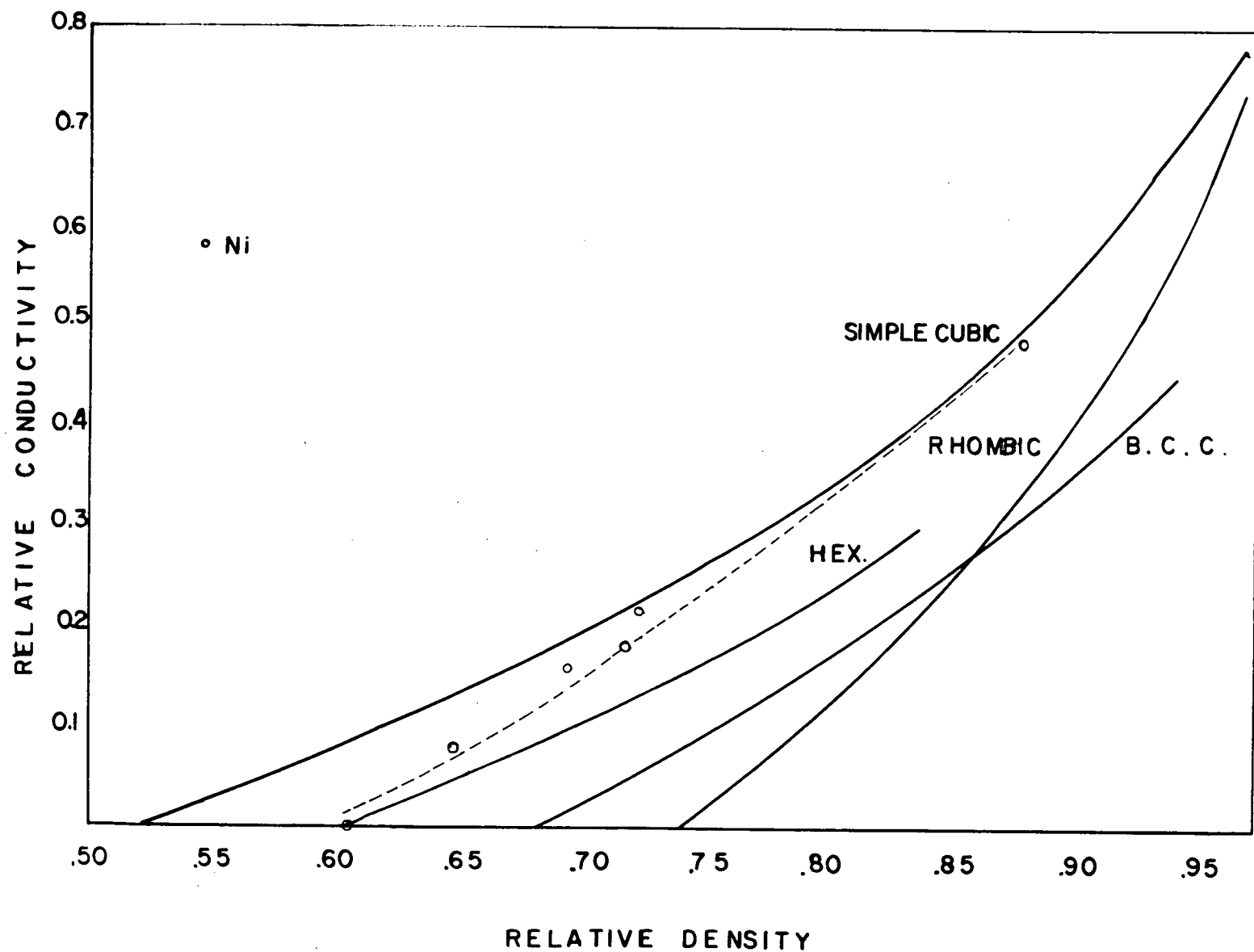
Figure 34. Corrected values of relative conductivity vs. relative density for nickel compacts.

order to do this, the work of Grootenhuis appears to be the logical choice, as both density and resistivity values were reported in his work. Other resistivity data were mostly reported as a function of temperature and pressure and thus could not be tested with the theoretical equation. Some of the results of Grootenhuis shown earlier in Figures 4 to 6 are replotted in Figure 35 and compared with the curves drawn from the present theory. The curve for orthorhombic packing is corrected for the zero-error and shifted upwards. A reasonable agreement with the experimental data can be seen, which again confirms the validity of the derived equation.

IV.8. PACKING GEOMETRY INSIDE THE DIE

It is evident from the Figures 30 to 34, that the experimental data follow closely the theoretically derived equation for the hexagonal prism model in the initial stages of densification. This agreement indicates that the overall packing geometry of spheres inside the die may be similar to the orthorhombic packing.

When a die is randomly filled with a number of monosized spheres, with intermittent shaking and tapping in order to achieve a uniform packing, the spheres tend to spread laterally to achieve the most stable configuration. However, the die-wall offers resistance to lateral spreading. As a result, a certain degree of stability of packing is maintained inspite of an unstable configuration. McGeary[31] studied the various modes of filling the die and the effect of container size on the packing density. His results are shown in Figure 36. At $\frac{D}{d}$ values greater than 10, the packing density of the compact reaches
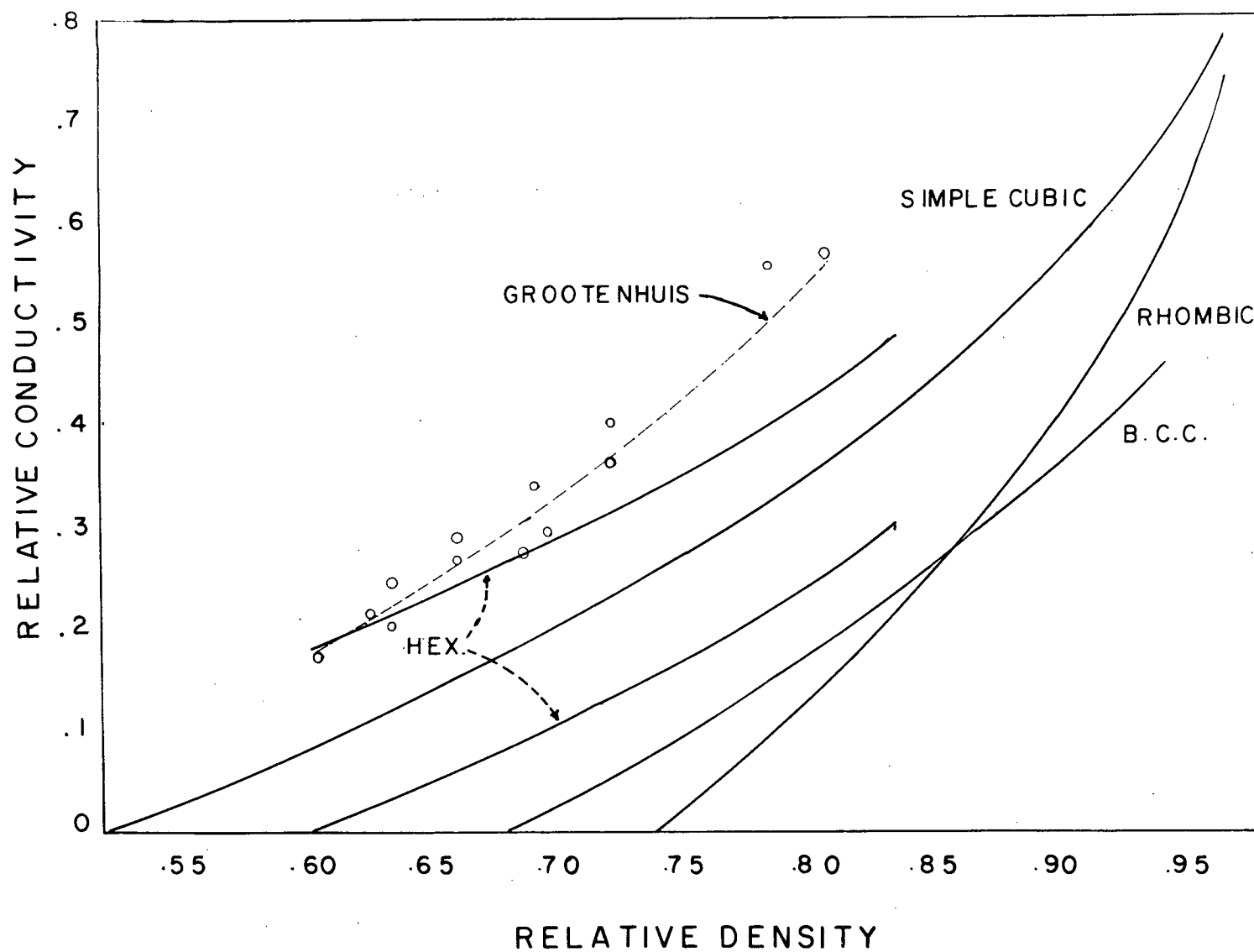
Figure 35. Results of previous investigations compared with proposed models.
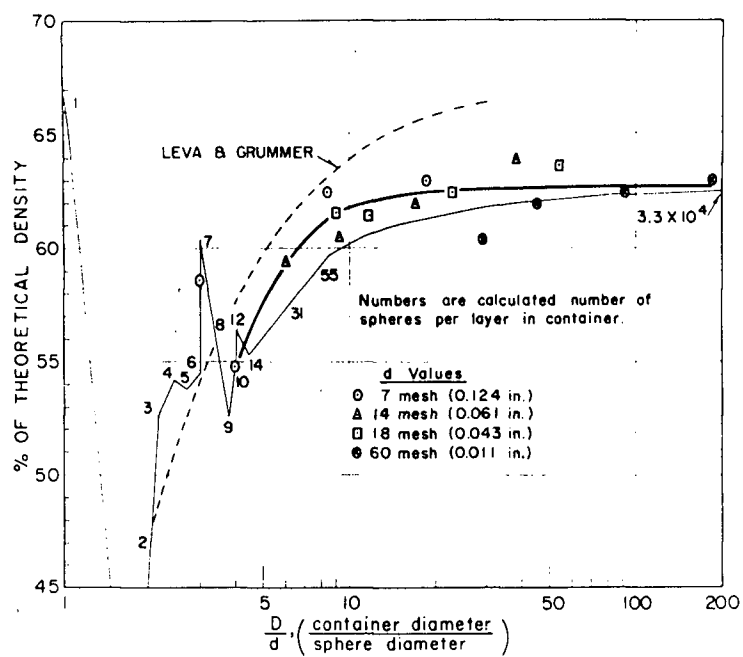
Figure 36. Effect of container size on the efficiency of
packing one-size spheres (After McG eary[31]).

a maximum of 62.5% of the theoretical density. This value is close to the as-compacted density for orthorhombic packing.

Smith, Foote and Busang[32] studied the coordination number of spheres in a die resulting after shaking and tapping. Their results showed a Gaussian distribution of the number of spheres with a given coordination number. The average coordination number of the spheres was close to 8. Thus these results confirm that the initial packing of the spheres inside a die is close to orthorhombic, as was observed in this study.

IV.9. DEFORMATION GEOMETRY INSIDE THE DIE

The width of the die does not permit an integral number of spheres across the diameter; hence the four ideal modes of packing discussed in section II do not exist across the diameter of the die, since a certain number of spheres are lightly held against the die-wall (due to the die-wall effect). On initial application of the load, the loosely held spheres rearrange, giving rise to a higher relative density. Duffield and Grootenhuis[33], and Kakar and Chaklader[34] reported a volume change of 1 to 4% for glass spheres of 0.5 mm average diameter, when a load of 1000 p.s.i. was applied at room temperature. As no particle (sphere) fragmentation was observed, this volume change was attributed to the particle rearrangement discussed above.

On further loading, the particles begin to deform. Kakar and Chaklader[34] studied the deformation geometry of spheres in randomly filled dies. Although individual colonies of rhombohedral or tetragonal deformation were observed, the majority of the spheres showed

a hexagonal prism mode of deformation. The mean coordination number of spheres during deformation was between 8 and 9. This indicates that the orthorhombic packing configuration is maintained during the initial stages of deformation, as was observed in the present study.

IV.10. EFFECTS OF OTHER PARAMETERS ON CONDUCTIVITY MEASUREMENTS

a) Surface Effect

Surface conduction has been known to affect the electrical conductivity measurements of dielectric materials. At temperatures below $300^{\circ}C$, the elctrical conductivity of glass is greatly influenced by its surface condition. Traces of water on the surface drastically increases the conductivity of glass[28]. Above $300^{\circ}C$, the contribution of the surface conductivity to the total conductivity becomes less significant, as the ionic conductivity of glass increases markedly. The surface to volume ratio also affects the surface conductivity, but for spheres this ratio has the minimum value and hence, the surface conductivity can be expected to be minimum for the compacts of spherical particles. The specific surface area (i.e. Cm^2/gm) of a particulate compact has the most significant effect on the surface conductivity, as compacts of very fine particles will have a large surface area available for conduction. In order to minimize the contribution from surface conduction on the overall conductivity, large spheres (0.4 to 0.6 mm diameter) of glass were used for conductivity measurements.

b) Orientation Effect

As previously discussed in the theoretical models,

$$\frac{\sigma_m}{\sigma_c} = \frac{A_c}{A_s} \cdot \frac{L_s}{L_c} \quad - - - - - - - - - - - - \quad (12)$$

This equation reduces to

$$\frac{\sigma_m}{\sigma_c} = \frac{A_c}{A_s} \quad ,$$

since in all four models, $L_c = L_s$. The direction of current-flow in

the models discussed has been considered to be perpendicular to the face

of the unit cells. In practice, however, one has to consider cases when

the current-flow is parallel to the face-diagonal or the cube-diagonal

of the unit cells. When the orientations of the unit cells are varied

with respect to the direction of current-flow, the number of paths

through the unit cell changes, but so do the effective area of current-

flow and the area of the unit cell normal to current-flow. The total

effect of the change of orientation with respect to the direction of

current-flow is such, that the conductivity of the unit cell is unaltered

regardless of its orientation, as shown in the appendices. Hence,

the resistivity of systematically packed spheres does not change with

the direction of current-flow. However, the packing of spheres inside

a die is not systematic, and this could cause large variations in

conductivity depending on the direction of current-flow. Any change

in the position of neighbours of a given sphere from the ideal configuration

could increase or decrease the number of current-paths and the effective

area of current-flow. The conductivity is a very sensitive function

of packing geometry. The results obtained in the present-work on glass

and nickel only indicate that any such deviations due to random filling

apparently nullify one another. Thus, the overall conductivity-density

relationship follows the orthorhombic model reasonably well.

V. SUMMARY AND CONCLUSIONS

The electrical resistivity of a powder-compact during hot-pressing is calculated using the geometry of deformation of particles under load. The particles are assumed to be monosized spheres. An equation relating the electrical conductivity to the relative density for different ideal packing arrangements has been derived, which is $\sigma_m/\sigma_c = \alpha \; (D^{2/3} \; \beta^{2/3} \; R^2 - 1)$. The theoretical equation was compared with hot-pressing data on glass and nickel spheres. The following conclusions can be made.

1) The general theoretical equation proposed is found to be obeyed by the particles during the initial stages of hot-pressing (in the range 0.65 to 0.75 relative density).

2) A deviation in the range 0.6 to 0.65 relative density was encountered, which could be due to particle rearrangement at the beginning of hot-pressing.

3) The relative conductivity vs. relative density plots showed that the overall packing of spheres inside the die is close to orthorhombic, in agreement with the observations of previous studies.

4) The theoretical equation has been modified in order to take into account the relative conductivity of the green compact. The modified equation fits the data on metal-compacts obtained in the present study and in previous investigations.

VI. SUGGESTIONS FOR FUTURE WORK

1)   It would be interesting to derive the resistance of a sphere in terms of the contact areas from potential theory and La Place's equation in three-dimensions. This will give an equation which would predict the resistance of the green-compact as well as the resistance during deformation.

2)   The coordination change in the initial stages of hot-pressing could be closely followed by evaluating any change in the parameter 'α' in this range.

3)   The theoretical equation could be tested with more resistivity data of random-shaped particles. Similarly, the particle size effect on the relative conductivity should be experimentally determined and its effect on the theoretical predictions should be evaluated.

APPENDICES

There are five simple and systematic modes of packing of

uniform spheres. These are shown in Figure 37 (from Morgan[35]) and

can be described as follows.

1. Cubic Packing

This packing is constructed by placing spheres in square

formation (figure 37a). Spheres in second and subsequent layers are

placed vertically over those in preceding layers. Such an arrangement

makes this packing most open and least stable.

2. Orthorhombic Packing

Figure 37 c and d shows that this type of packing can be

obtained either be stacking spheres in second layer horizontally, offset

with respect to those in the first layer by a distance R (sphere radius)

along the direction of one set of rows, or by stacking vertically over those

in first simple rhombic layer. It turns out that these two ways of packing

are identical in nature, though of different orientation in space.

3. Body-Centred-Cubic Packing

Figure 37 b shows this type of packing. It can be seen that

if the spheres in the third layer have to lie vertically over those in

the first, it forms a very unstable arrangement in a unidirectional

force field.

4. Tetragonal Packing

This is constructed by placing spheres in second layer horizontally,

offset with respect to those of the first layer by a distance R, along the

direction of one of the sets of rows. All the layers are simple rhombic in this case.

5. Rhombohedral Packing.

As in the case of orthorhombic packing, this can be constructed either from square-layer type base, or from simple rhombic-layer type base. But in this case, the spheres in second layer are horizontally offset with respect to those in the first layer. This offset is in a direction bisecting the angle between two sets of rows by a distance of $R\sqrt{2}$ in the case of square layer formation, and of $2R/\sqrt{3}$ in the case of simple rhombic layer formation. These two ways of packing are identical in nature, though of different orientation in space.

Table III summarises the basic methods of simple and systematic packing of uniform spheres.

TABLE III

Basic Methods of Packing and their Construction

Method of Packing	Coordination Number	Density %
Simple Cubic	6	52.36
Orthorhombic	8	60.46
Body-Centred-Cubic	8	68.02
Tetragonal	10	69.81
Rhombohedral	12	74.05
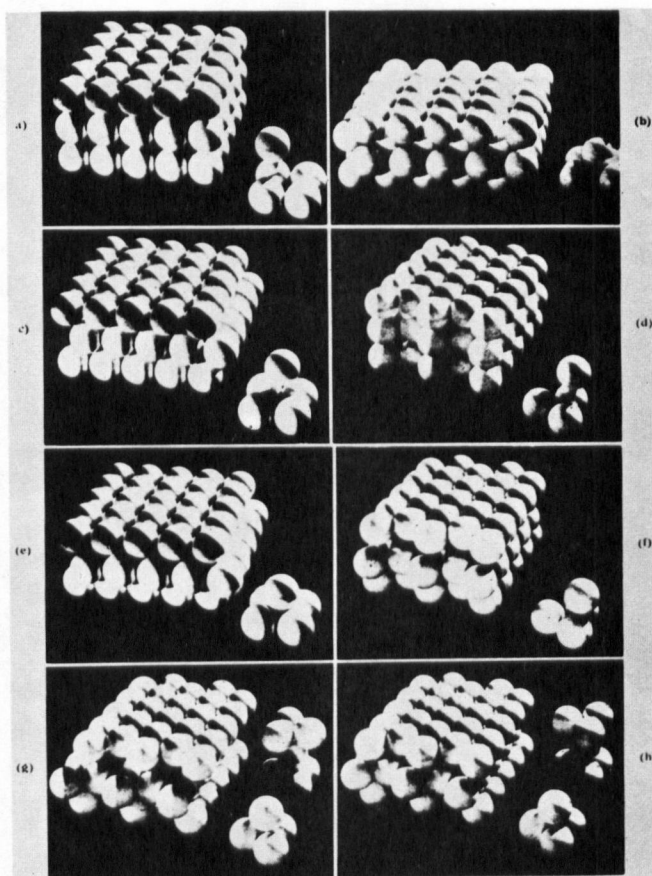
(a) Cubic

(b) Body-centered cubic

(c) Orthorhombic
     (from cubic base).

(d) Orthorhombic
     (from rhombic base).

(e) Rhombohedral
     (from cubic base;
      face-centred cubic).

(f) Tetragonal.

(g) Rhombohedral
     (from rhombic base;
      face-centred cubic).

(h) Rhombohedral
     (from rhombic base;
      close-packed hexagonal).

Figure 37. Basic systems of spherical packings (After Morgan[35]).

APPENDIX II

A. Theoretical Calacuations

The theoretical values are calculated using equation(23)for different packing arrangements.

$$\frac{\sigma_m}{\sigma_c} = \alpha \; (D^{2/3} \; \beta^{2/3} \; R^2 - 1) \qquad ------ (23)$$

Equation(21)is the same equation as above for $\frac{a}{R} < 0.25$.

$$\frac{\sigma_m}{\sigma_c} = \alpha \left[\left(\frac{D}{D_o} \right)^{2/3} - 1 \right] \qquad ------ (21)$$

Values of R and D for different $\frac{a}{R}$ ratios are read from Figure 18 (which gives R values) and Figure 38 (which gives D values), respectively. (Ref. 26). R has arbitrary units.

Values of α, β, and D_o for different packings are given in Table II (Chapter II).
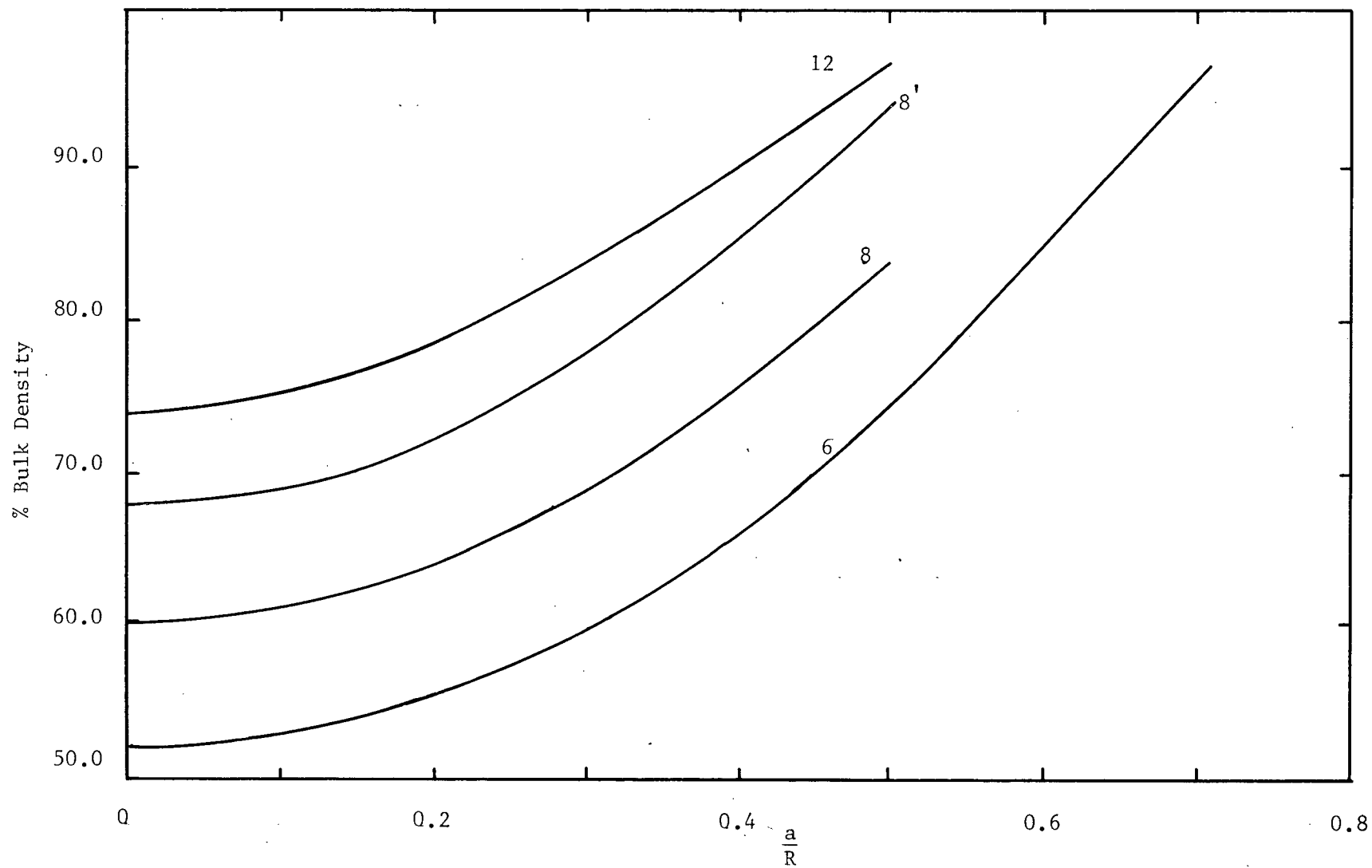
Figure 38. Theoretical relationship of D vs. a/R for the proposed models (After Kakar[26]).

1. Simple Cubic Packing

$\frac{a}{R}$	R	$D_\%$	$\frac{\sigma_m}{\sigma_c}$
0	0.620	52.36	0
0.05	0.620	52.56	0.002
0.10	0.620	53.15	0.008
0.15	0.620	54.15	0.018
0.20	0.620	55.57	0.033
0.25	0.621	57.42	0.052
0.30	0.622	59.75	0.078
0.35	0.624	62.58	0.110
0.40	0.627	65.94	0.150
0.45	0.631	69.87	0.199
0.50	0.637	74.39	0.262
0.55	0.646	79.59	0.341
0.60	0.660	85.09	0.442
0.65	0.679	90.84	0.575
0.70	0.710	95.94	0.755

2. Orthorhombic Packing

$\dfrac{a}{R}$	R	$D_\%$	$\dfrac{\sigma_m}{\sigma_c}$
0	0.620	60.46	0
0.15	0.620	62.51	0.021
0.20	0.620	64.12	0.038
0.25	0.622	66.21	0.061
0.30	0.623	68.77	0.090
0.35	0.625	71.82	0.127
0.40	0.629	75.34	0.173
0.45	0.635	79.27	0.230
0.5	0.643	83.51	0.302

3. Rhombohedral Packing

$\dfrac{a}{R}$	R	$D_\%$	$\dfrac{\sigma_m}{\sigma_c}$
0	0.620	74.05	0
0.15	0.620	76.53	0.051
0.2	0.621	78.44	0.093
0.25	0.622	80.84	0.148
0.30	0.624	83.70	0.220
0.35	0.628	86.91	0.310
0.40	0.633	90.32	0.432
0.45	0.642	93.65	0.564
0.50	0.656	96.41	0.741

4. B.C.C. Packing

$\frac{a}{R}$	R	$D_\%$	$\frac{\sigma_m}{\sigma_c}$
0	0.620	68.02	0
0.15	0.620	70.33	0.031
0.2	0.620	72.14	0.057
0.25	0.622	74.48	0.091
0.30	0.623	77.37	0.135
0.35	0.625	80.80	0.190
0.40	0.629	84.76	0.259
0.45	0.635	89.18	0.345
0.50	0.643	93.95	0.454

B. EXPERIMENTAL RESULTS

1. Glass at 550°C

a = 0.70 mm average diameter; b = 0.42 mm average diameter

$$D_o = 0.632 \; ; \; \sigma_c = 1.27 \times 10^{-3} \; \text{ohm}^{-1} - \text{Cm}^{-1}$$

$\sigma_m \times 10^{-5}$ $\text{ohm}^{-1}\text{cm}^{-1}$		D		$\left[\left(\dfrac{D}{D_o} \right)^{2/3} - 1 \right] \times 10^{-2}$		$\dfrac{\sigma_m}{\sigma_c}$	
a	b	a	b	a	b	a	b
1.54	1.60	0.658	0.645	2.94	1.58	0.012	0.013
2.76	3.57	0.661	0.650	3.25	2.11	0.022	0.028
3.71	7.34	0.664	0.662	3.57	3.36	0.029	0.058
5.80	9.31	0.670	0.671	4.19	4.29	0.046	0.073
7.33	10.70	0.673	0.677	4.50	4.91	0.058	0.084
8.67	11.88	0.679	0.687	5.12	5.94	0.068	0.094
13.41	14.80	0.701	0.703	7.38	7.58	0.106	0.117
14.09	15.89	0.712	0.707	8.50	7.99	0.111	0.125
16.76	17.34	0.725	0.721	9.82	9.41	0.132	0.137
18.04	21.47	0.733	0.75	10.06	12.33	0.142	0.169
18.53	24.13	0.74	0.765	11.33	13.52	0.146	0.189
20.23	27.09	0.751	0.78	12.43	14.31	0.16	0.213

2. Glass at $600^{\circ}C$

$$D_o = 0.64 \qquad\qquad \sigma_c = 3.5 \times 10^{-3} \text{ ohm}^{-1}\text{-cm}^{-1}$$

$\sigma_m \times 10^{-4}$ ohm^{-1}cm^{-1}		D		$\left[\left(\dfrac{D}{D_o}\right)^{2/3} - 1\right] \times 10^{-2}$		$\dfrac{\sigma_m}{\sigma_c}$	
a	b	a	b	a	b	a	b
0.40	0.19	0.657	0.644	1.71	0.46	0.011	0.005
1.13	0.81	0.660	0.661	2.07	2.21	0.031	0.023
2.56	1.76	0.678	0.67	3.92	3.1	0.071	0.049
3.03	2.20	0.687	0.675	4.84	3.56	0.084	0.062
3.81	3.09	0.692	0.690	5.35	5.16	0.106	0.087
4.79	4.81	0.724	0.728	8.57	8.97	0.133	0.136
5.44	5.28	0.737	0.738	9.87	9.91	0.151	0.15

3. Glass at 650°C

$$D_o = 0.63 \qquad\qquad \sigma_c = 6.45 \times 10^{-3} \text{ ohm}^{-1}\text{-cm}^{-1}$$

$\sigma_m \times 10^{-4}$ $\text{ohm}^{-1}\text{cm}^{-1}$		D		$\left[\left(\dfrac{D}{D_o}\right)^{2/3} - 1\right] \times 10^{-2}$		$\dfrac{\sigma_m}{\sigma_c}$	
a	b	a	b	a	b	a	b
2.43	1.62	0.667	0.665	3.88	3.67	0.037	0.026
3.65	3.47	0.676	0.678	4.81	5.02	0.056	0.055
4.85	5.95	0.684	0.691	5.64	6.36	0.074	0.095
6.42	6.72	0.695	0.700	6.77	7.28	0.098	0.107
7.71	7.74	0.714	0.712	8.70	8.50	0.118	0.123
8.65	8.34	0.724	0.722	9.72	9.51	0.132	0.133
9.26	12.35	0.731	0.778	10.42	15.11	0.141	0.196
10.75	12.61	0.752	0.79	12.53	16.29	0.164	0.200

4. Nickel at Room Temperature

$$\sigma_c = 14.62 \times 10^4 \quad \text{ohm}^{-1} \text{ cm}^{-1}$$

σ_m ohm^{-1} cm^{-1} x 10^4	D	$\dfrac{\sigma_m}{\sigma_c}$
2.63	0.602	0.180
3.79	0.646	0.259
4.87	0.688	0.333
4.95	0.692	0.339
5.34	0.715	0.365
5.95	0.720	0.407
9.8	0.877	0.67

APPENDIX III

THEORETICAL MODELS FOR DIFFERENT ORIENTATIONS OF THE UNIT CELL

1) Simple Cubic Packing

Consider the current-flow along a face-diagonal (Figure 39a).

Number of current-paths = 2 .

Area of current-flow $= 2\pi a^2 \times \dfrac{1}{\sqrt{2}} = A_c$.

Area of the unit cell normal to current flow $= 4\sqrt{2}\, y^2$.

$$\therefore \quad \frac{\sigma_m}{\sigma_c} = \frac{A_c}{A_s}$$

$$= \frac{\sqrt{2}\, \pi a^2}{4\sqrt{2}\, y^2}$$

$$= \frac{\pi}{4} \frac{a^2}{R^2 - a^2} \quad .$$

2) Orthorhombic Packing

Consider the current-flow normal to a prism-face (Figure 39b).

Number of current-paths through the unit cell = 3;
one path lies completely inside the unit cell and the other two are
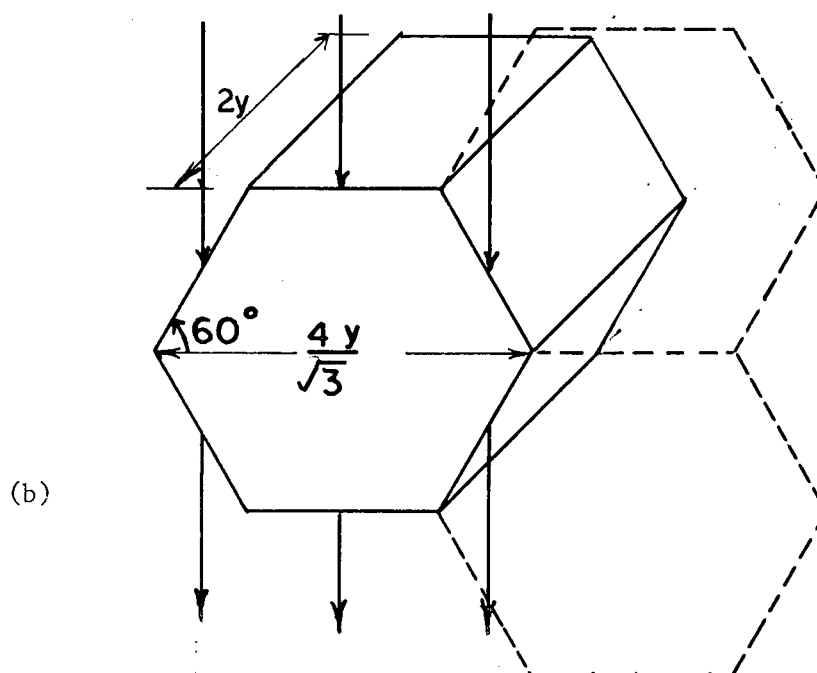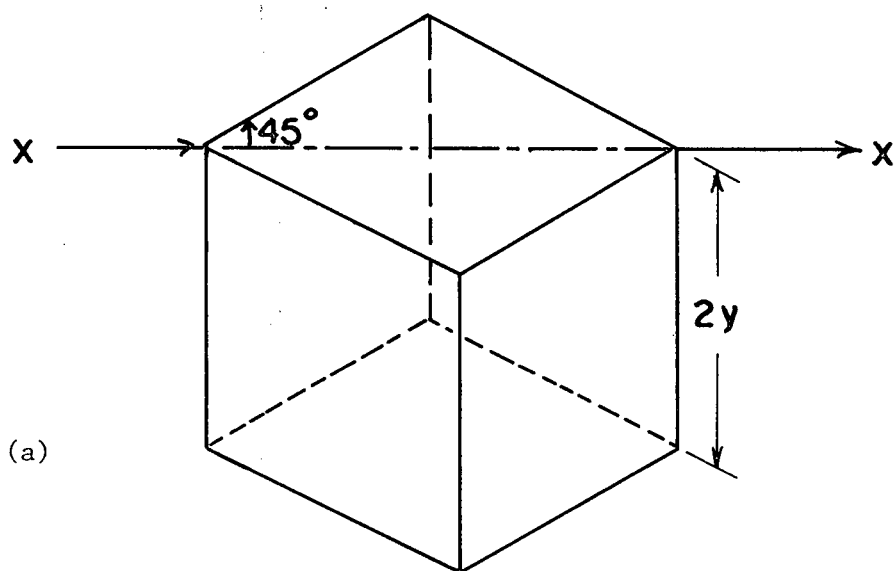shared by three unit cells a-piece.

Figure 39. Geometric relationships for the unit-cells, in different orientations with respect to current path.

Hence effective area of current-flow through the unit cell

$$= \pi a^2 + \frac{2}{3} \pi a^2 \cos \theta, \quad \text{where}$$

$$\cos \theta = \frac{1}{2}, \text{from geometry.}$$

Hence

$$A_c = \pi a^2 + \frac{1}{3} \pi a^2$$

$$= \frac{4}{3} \pi a^2 \quad .$$

$$A_s = \frac{4y}{\sqrt{3}} \times 2y \; .$$

$$\therefore \quad \frac{\sigma_m}{\sigma_c} = \frac{A_c}{A_s}$$

$$= \frac{4}{3} \quad \frac{\pi a^2}{\frac{4}{\sqrt{3}} \, 2y^2} \quad = \quad \frac{\pi}{2\sqrt{3}} \quad \frac{a^2}{R^2 - a^2} \quad .$$

3) Rhombohedral Packing

Consider an F.C.C. unit cell. Let the current-flow be parallel to the edge (Figure 39c).

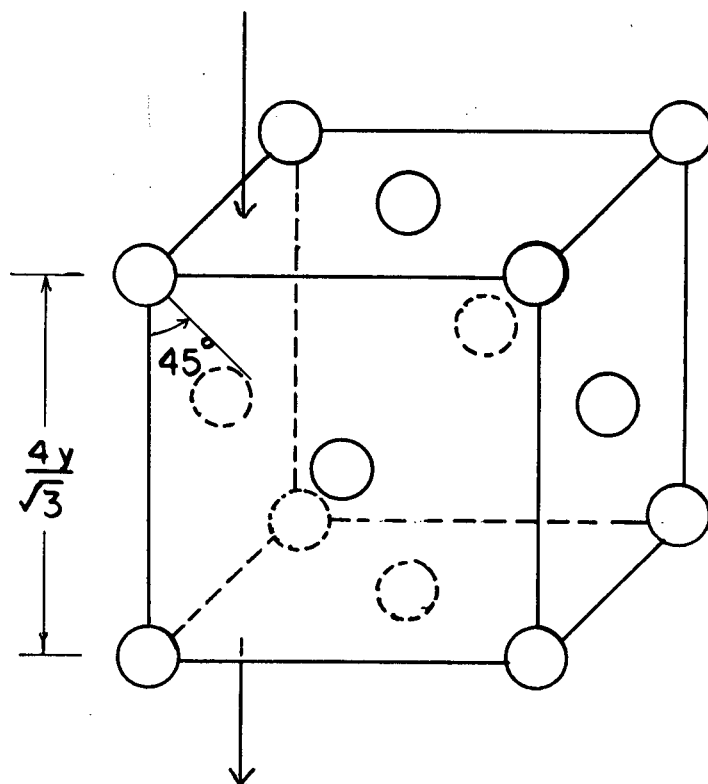Effective number of current-paths = 8 .

$\therefore$ Area of current-flow is

$$= 8\pi a^2 \cos \theta , \quad \text{where}$$

$$\cos \theta = \frac{1}{\sqrt{2}} \; \text{,from geometry.}$$
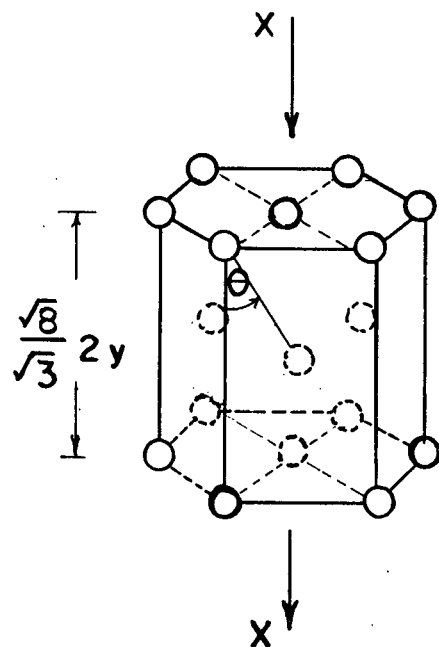
$$A_s = 8y^2 \quad .$$

39 (c)

39 (d)

Figure 39. (c & d).Geometric relationships for the unit-cells in
different orientations with respect to current path

Hence
$$\frac{\sigma_m}{\sigma_c} = \frac{A_c}{A_s} \quad .$$

i.e.
$$\frac{\sigma_m}{\sigma_c} = 8\pi a^2 \times \frac{1}{\sqrt{2}} \times \frac{1}{8y^2}$$

$$= \frac{\pi}{\sqrt{2}} \quad \frac{a^2}{R^2 - a^2} \quad .$$

4) <u>Alternative Approach for H.C.P. Packing</u>

From Figure 39d,

Number of current-paths = 9 ..

$$A_c = 9\pi a^2 \cos \theta, \qquad \text{where}$$

$$\cos \theta = \frac{\sqrt{2}}{\sqrt{3}} \text{ , from geometry;}$$

and
$$A_s = 6\sqrt{3} \ y^2 ..$$

$$\therefore \quad \frac{\sigma_m}{\sigma_c} = \frac{A_c}{A_s} = 9\pi a^2 \quad \frac{\sqrt{2}}{\sqrt{3}} \quad \frac{1}{6\sqrt{3} \ y^2}$$

$$= \frac{\pi}{\sqrt{2}} \quad \frac{a^2}{R^2 - a^2} \quad .$$

5) <u>Alternative Approach for B.C.C. Packing</u>

Consider the current-flow along the edge (Figure 39e).

Number of current-paths = 4 .

$$A_c = 4\pi a^2 \text{ x } \cos \theta \text{ , where}$$

$$\cos \theta = \frac{1}{\sqrt{3}} \text{ from geometry;}$$

and

$$A_s = \frac{16y^2}{3} \text{ .}$$

$$\therefore \quad \frac{\sigma_m}{\sigma_c} = \frac{A_c}{A_s} = \frac{4\pi a^2}{\sqrt{3}} \text{ x } \frac{3}{16y^2}$$

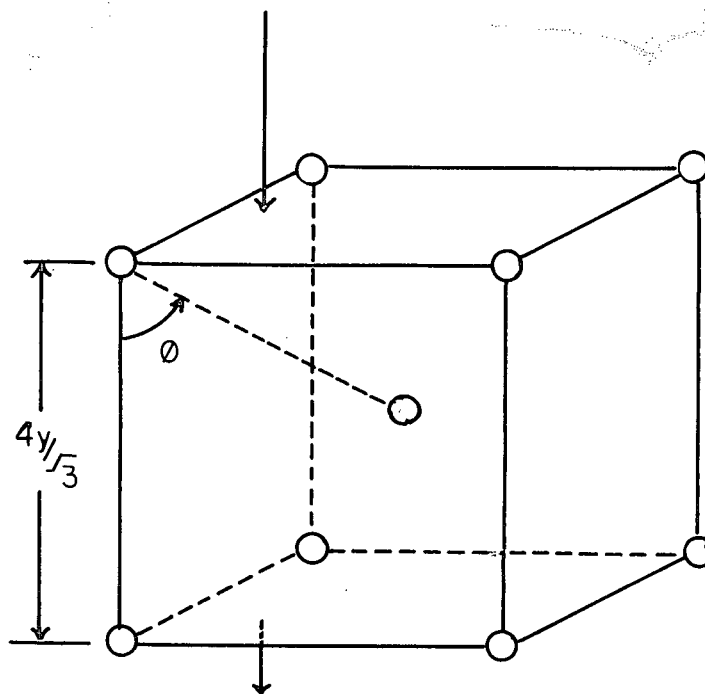$$= \frac{\sqrt{3}}{4} \pi \frac{a^2}{R^2 - a^2}_{o} \text{ .}$$

Consider current-flow along the face diagonal (Figure 39f).

Number of paths through the unit cell = 2 .

$$A_c = 2\pi a^2 \cos \theta \text{ , and } \cos \theta = \frac{\sqrt{2}}{\sqrt{3}} \text{ , from geometry.}$$

$$A_s = \frac{4y}{\sqrt{3}} \text{ x } \frac{\sqrt{2} \ 2y}{\sqrt{3}} = \frac{8\sqrt{2} \ y^2}{3}$$
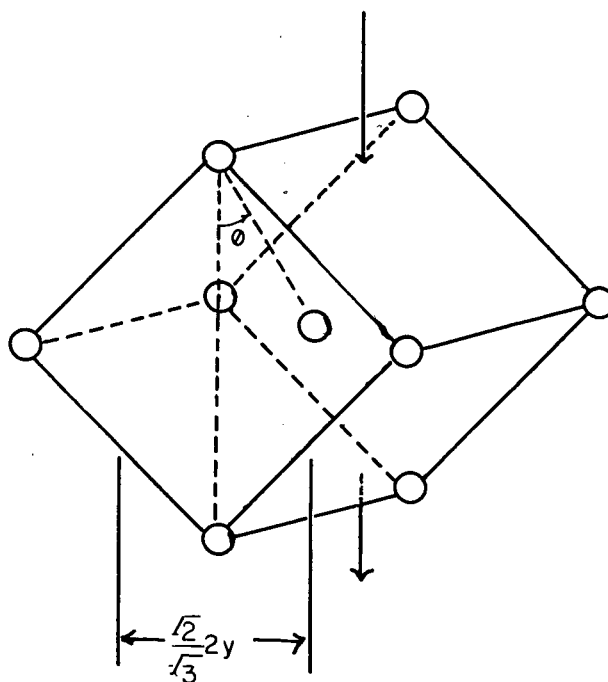
39 (e)

39 (f)

Figure 39. (e & f). Geometric relationships for the unit-cells in
different orientations with respect to current path.

$$\frac{\sigma_m}{\sigma_c} = \frac{A_c}{A_s}$$

$$= 2\pi a^2 \ x\frac{\sqrt{2}}{\sqrt{3}} \ \cdot \ \frac{3}{8\sqrt{2} \ y^2}$$

$$= \frac{\sqrt{3}}{4} \ \pi \ \frac{a^2}{y^2} \ .$$

BIBLIOGRAPHY

1. "Sintering and Related Phenomena". Eds. G. C. Kuczynski, N. A. Hooton,and C. F. Gibbon, (1965).

2. P. Murray, D. T. Livey, and J. Williams, "Ceramic Fabrication Processes", Ed. W. D. Kingery, 147-170 (1963).

3. W. Trzebiatowski, Z. Physik. Chem., A169, 91 (1934).

4. K. Iwase and K. Ogawa, J. Japan Soc.Powder Met., 1, 1 (1947).

5. R. H. Myers, Metallurgia, 38, 307 (1948).

6. G. F. Huttig, Kolloid Z., 98(3), 263 (1942).

7. K. Adlassnig and O. Foglar, Radex-Rundschau, 2, 79 (1950).

8. H. H. Hausner and J. H. Dedrick, "Physics of Powder Metallurgy", Ed. W. Kingston, 320 (1951).

9. T. Kimura and H. Hisamatsu, Planseeber. Pulvermet., Bd.14, 85 (1966).

10. P. Grootenhuis, R. W. Powell and R. P. Tye, Proc. Phys. Soc. (London), B65, 502 (1952).

11. C. G. Goetzel, J. Inst. Met., 66, 319 (1940).

12. F. R. Hensel, E. I. Larsen and E. F. Swazy, Metals Technology, 12(5), 1810 (1945).

13. R. Kieffer and W. Hotop, Kolloid Z., 104, 208 (1943).

14. F. Sauerwald and St. Kubik, Z. Elektrochem., 38, 33 (1932).

15. G. Grube and H. Schlecht, Z. Elektrochem., 44, 367 (1938).

16. Lord Raleigh (J. Maxwell), Phil. Mag., 34, 481 (1892).

17. H. J. Juretschke, R. Landauer, and J. A. Swanson, J. Appl. Phys., 27, 838 (1956).

18. W. Doebke, Z. Tech. Physik., 11, 12 (1930).

19. K. Torkar, Chem. Ingr. Tech., 25, 308 (1953).

20. R. B. Grekila and T. Y. Tien, J. Am. Cer. Soc., 48, 22 (1965).

21. E. Klar and A. B. Michael, Trans. AIME, 242, 2173 (1968).

22.   G. F. Huttig, Z. Electrochem., <u>54</u>, 89 (1950).

23.   P. I. Mal'ko, V. F. Nemchenko, and S. N. L'vov, Porosh. Met.,
<u>7</u>, 55 (1968).

24.   P. P. Litvinenko, Trudy. Kuibyshevsk. Aviats. Inst., <u>26</u>, 76 (1962).

25.   V. I. Odelevskii, Zh. Tekhn. Fiz., <u>26</u>, 667 (1951).

26.   A. K. Kakar, "Deformation Theory of Hot-pressing", Ph.D. Thesis,
Dept. Metallurgy, U.B.C. (1967).

27.   L. C. Graton and H. Fraser, J. Geol., <u>43</u>, 785 (1935).

28.   W. Morey, "Properties of Glass", 474-480 (1954).

29.   R. Terai, Phys. Chem. Glasses, <u>10</u>(4), 146 (1969).

30.   H. Kaneko and J. O. Isard, Phys. Chem. Glasses, <u>9</u>(3), 84 (1968).

31.   R. K. McGeary, J. Am. Ceram. Soc., <u>44</u>, 513 (1961).

32.   W. O. Smith, P. D. Foote, and P. F. Busang, Phys. Rev., <u>34</u>,
1272 (1929).

33.   A. Duffield and P. Grootenhuis, Special Report no. 58, pp.96,
Symposium on Powder Metallurgy (Iron and Steel Institute), (1954).

34.   A. K. Kakar and A. C. D. Chaklader, J. App. ~~Sci~~. Phys., <u>38</u>(8), 3223 (1967).

35.   V. T. Morgan, Special Report no. 58, pp. 86, Symposium on Powder
Metallurgy,(Iron and Steel Institute),(1954).